wind

MDPI

Article

Wind Estimation Methods for Nearshore Wind Resource Assessment Using High-Resolution WRF and Coastal Onshore Measurements

Taro Maruo * and Teruo Ohsawa

Graduate School of Maritime Sciences, Kobe University, 5-1-1 Fukae-minami-machi, Higashinada-Ku, Kobe 658-0022, Japan
* Correspondence: 198w314w@stu.kobe-u.ac.jp

Abstract

Accurate wind resource assessment is essential for offshore wind energy development, particularly in nearshore sites where atmospheric stability and internal boundary layers significantly influence the horizontal wind distribution. In this study, we investigated wind estimation methods using a high-resolution, 100 m grid Weather Research and Forecasting (WRF) model and coastal onshore wind measurement data. Five estimation methods were evaluated, including a control WRF simulation without on-site measurement data (CTRL), observation nudging (NDG), two offline methods—temporal correction (TC) and the directional extrapolation method (DE)—and direct application of onshore measurement data (DA). Wind speed and direction data from four nearshore sites in Japan were used for validation. The results indicated that TC provided the most accurate wind speed estimate results with minimal bias and relatively high reproducibility of temporal variations. NDG exhibited a smaller standard deviation of bias and a slightly higher correlation with the measured time series than CTRL. DE could not reproduce temporal variations in the horizontal wind speed differences between points. These findings suggest that TC is the most effective method for assessing nearshore wind resources and is thus recommended for practical use.

Keywords: wind resource assessment; nearshore; weather research and forecasting model; on-site measurement; spatial extrapolation; offline method

check for updates

Academic Editor: Giuseppe Failla

Received: 1 April 2025
Revised: 30 June 2025
Accepted: 1 July 2025
Published: 7 July 2025

Citation: Maruo, T.; Ohsawa, T. Wind Estimation Methods for Nearshore Wind Resource Assessment Using High-Resolution WRF and Coastal Onshore Measurements. *Wind* **2025**, *5*, 17. https://doi.org/10.3390/wind5030017

Copyright: © 2025 by the authors. Licensee MDPI, Basel, Switzerland. This article is an open access article distributed under the terms and conditions of the Creative Commons Attribution (CC BY) license (https://creativecommons.org/licenses/by/4.0/).

1. Introduction

Accurate and precise wind resource assessments are essential as they form the basis for energy yield assessments used in financial evaluations during the planning stage of wind farms. In these assessments, on-site wind data measured at specific points ("measurement point" or "reference point") are spatially extrapolated to the position of planned wind turbines ("target points") based on wind fields simulated by a wind flow model, and during the planning stage of a wind farm, the wind conditions within a radius of approximately 10 km around the reference point are estimated [1].

In recent years, the development of offshore wind farms in Japan has accelerated, particularly in nearshore areas located just a few kilometers from the shoreline [2]. Due to the high cost of constructing offshore meteorological masts, it is a common practice in the early stages of development to conduct wind measurements onshore and extrapolate the conditions to offshore target points using numerical simulation models.

In typical wind resource assessment at onshore sites, conducting steady-state calculations for 12 or 16 directions using a computational fluid dynamics (CFD) model as a wind flow model for wind resource assessment on land is standard practice. This is because the dominant factors that cause spatial variations in the wind field on land are the topography and surface roughness. Representative models include WAsP [3,4] in Europe, as well as MASCOT [5,6] and RIAM-COMPACT [7] in Japan.

On the other hand, at nearshore sites, the effects of atmospheric stability and internal boundary layers (IBLs), as well as the distribution of topography and surface roughness, are predominant [8]. The formation and structure of IBLs in coastal regions have been studied extensively for decades and are well-documented in the previous literature, including textbooks [8]. These studies have characterized the coastal IBL under both dynamical and thermodynamical influences. More recently, research into coastal discontinuities—including but not limited to IBLs—has advanced through the use of mesoscale meteorological simulations, in addition to site measurements and wind farm operational data [9–16]. These features influence wind structure in ways that CFD models—without thermodynamic processes—cannot adequately simulate. Therefore, the use of the Weather Research and Forecasting model (WRF) [17], a mesoscale meteorological model that can take into account thermodynamic processes, as a numerical simulation model for spatial extrapolation would be valuable. In fact, several studies [6,14–16] have demonstrated the usefulness of the mesoscale Weather Research and Forecasting (WRF) model, which incorporates thermodynamic processes, in simulating nearshore wind conditions more accurately.

WRF has the advantage of being able to reproduce three-dimensional meteorological fields and can generate time series data for wind speed and direction. However, WRF uses large-scale meteorological fields as input and does not reference in situ measurements, so the simulation result without intentional correction does not necessarily correspond to actual wind conditions. This study proposes a technique that corrects WRF values at offshore target points at each time step using the error vectors of WRF winds at the reference point. This technique is referred to as the time correction method (TC) in this paper.

To verify the effectiveness of TC, we also examined two other methods that combine WRF and in situ measurements, as well as two reference methods—one using WRF simulation data as-is (CTRL) and another using in situ measurements as-is (DA).

One of the combined methods mimics the approach commonly used in many CFD models. A CFD model outputs wind fields according to the direction of inflow, whereas the WRF outputs time series data on wind speed and direction by reproducing the three-dimensional meteorological field. Statistically processing the time series data output from WRF makes it possible to extrapolate spatially based on the wind field for each wind direction in the same way when the CFD model is used; this is referred to as the directional extrapolation method (DE) in this study.

The other method is observation nudging (NDG), which is one of the data assimilation techniques available in WRF [18]. This technique incorporates observational data into the model calculations in real time. Several studies have investigated its effectiveness in improving the accuracy of wind resource assessments [19,20]. Gryning et al. [19] showed that the observation nudging method reduced the root mean square error (RMSE) of wind speed; however, the impact on bias was minor. In this study, the reference (input) and estimation points were the same; therefore, the effect of the observation nudging method on the surrounding area was not investigated. Mylonas et al. [20] showed that the observation nudging method of multiple variables significantly improved model performance regardless of atmospheric stability and reduced the RMSE by approximately 27%, in which the distance between the reference and estimation points was approximately 140 km.

The objective of this study is to establish a wind resource assessment method for nearshore areas using high-resolution WRF simulations and coastal onshore measurements. As a promising approach, TC is proposed and evaluated by comparing it with four other methods. For the evaluation, measurement data from four Japanese nearshore sites, where an offshore wind farm is planned to be installed, were used.

The remainder of this paper is organized as follows. In Section 2, the measurements at four nearshore sites, the methods for estimating wind conditions at target points using measurement data from the reference point and WRF, and the indicators used to evaluate accuracy are described. Section 3 presents a comparison of the accuracy of wind condition estimates obtained using different estimation methods. Section 4 discusses the relationship between the reference and target points at the four nearshore sites. Section 5 presents a summary of this research and discusses the practical applicability of the wind condition estimation method that integrates on-site measurements with WRF as well as future research directions.

2. Materials and Methods

2.1. Sites and Measurement Data

In this study, we used data from wind measurement campaigns conducted at four coastal sites in Japan. The locations of these sites are shown in Figure 1. Noshiro, Yuri-Honjo, Sakata, and Mutsu-Ogawara are located in the Tohoku region in northern Japan. The first three sites face the Sea of Japan, whereas Mutsu-Ogawara faces the Pacific Ocean. Figure 2 illustrates the measurement points in each site. All of the sites are located along the coastline and exhibit a clear land–sea contrast in terms of topography and surface roughness. Table 1 presents the equipment, measurement heights, and installation details for each point, and Table 2 provides the assignments of the reference point and target points at the four sites for the examination cases. The information in Table 1; Table 2 is referred to in the following descriptions of each site based on Figure 2.

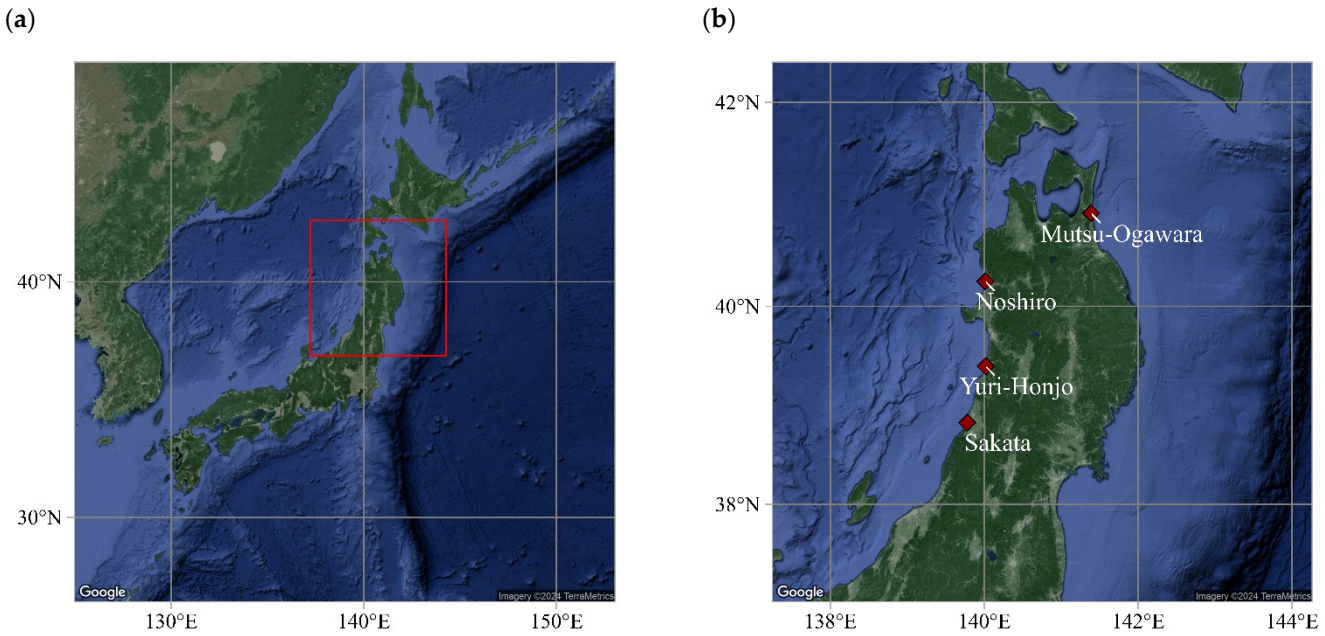


Figure 1. (**a**) Overview of Japan. (**b**) Locations of four coastal sites in Japan where wind measurement campaigns were conducted. The four sites are located in the red rectangle on the map on the left.

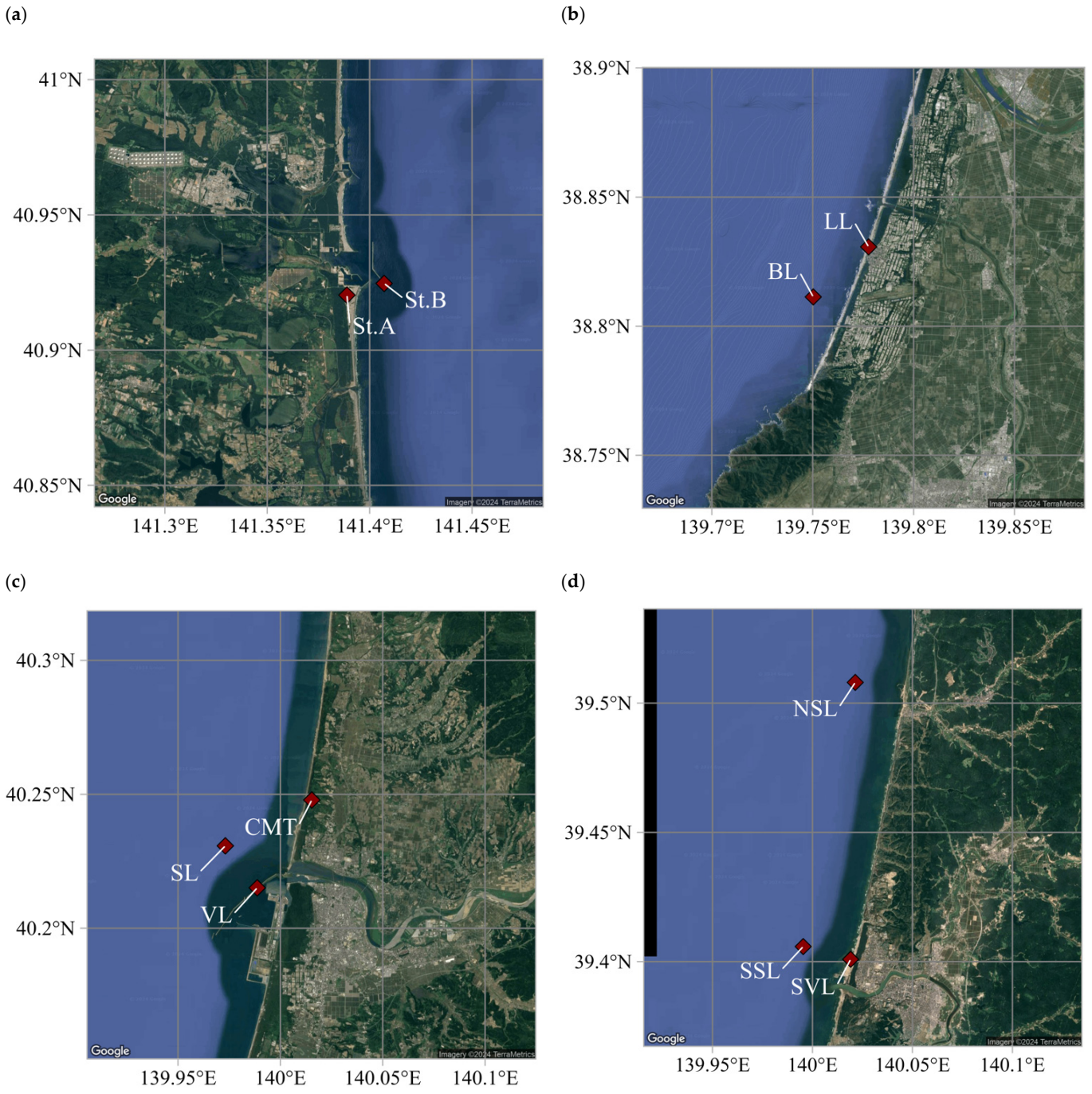


Figure 2. Measurement points in each site: (**a**) Mutsu-Ogawara, (**b**) Sakata, (**c**) Noshiro, and (**d**) Yuri-Honjo.

Table 1. Measurement configuration. AMSL: Above Mean Sea Level.; VL: Vertical (Doppler) LiDAR; SSL: Single Scanning (Doppler) LiDAR system; DSL: Dual Scanning (Doppler) LiDAR system; DBS: Doppler Beam Swinging; RHI: Range Height Indicator; VAD: Velocity Azimuth Display; CW: Continuous wave; PPI: Plan-Position Indicator; SR: Sampling Rate; LoS: Line-of-Sight.

Site	Point	Method	Scan	Equipment	Specification and Settings of Scan	Height Used for Analysis (from AMSL) [m]	Installation Situation
Mutsu-Ogawara	St. A	VL	DBS	Windcube V2.1	SR: 1 Hz (0.8 s/pulses) 4 inclined beams at 28° and 1 vertical beam Measured: 12 heights	50, 66, 87, 107, 127, 147, 167, 187, 207	On land
	St. B	VL	DBS	Windcube V2.1	Same as above	50, 120, 200	On breakwater
Sakata	LL	VL	DBS	DIABREZZA	Measured: 20 heights 4 inclined beams at 30° and 1 vertical beam	51.5, 71.5, . . ., 211.5	On land
	BL	VL	DBS	DIABREZZA	Same as above	53, 113, 173	On buoy
Noshiro	CMT	Cup and Vane	-	-	SR: 1 Hz Measured: 1 height	57.0	Installed meteorological mast on land
	SL	DSL	RHI	Windcube 200S×2	SR: 1 Hz Included Angle: 42.3° Gate Length: 50 m Measured: 3 heights	28, 115	On land, but measuring offshore point
	VL	VL	VAD (CW)	ZX LiDAR 300M	SR: 1 Hz Measured: 3 heights 50 LoS/1 s at 30° Measured: 8 heights	26, 113	On breakwater
Yuri-Honjo	SVL	VL	VAD (CW)	ZX LiDAR 300M	Same as above Measured: 5 heights	40, 100, 160	On land
	SSL	SSL	PPI	StreamLine XR	SR: 1 Hz Sector size: 60°, consisting of 5 LoS Gate Length: 90 m Measured: 3 heights	40, 100, 160	On land, but measuring offshore point
	NSL	SSL	PPI	StreamLine XR	Same as above	40, 100, 160	On land, but measuring offshore point

Table 2. Assignments of each point in the verification in this study, the distance from the reference point to the target point, and sample size. The distances between the shoreline and target point were approximate values, excluding breakwaters from land classification. * For St. A at Mutsu-Ogawara (Case 01–03), LL at Sakata (Case04–06), and SL and VL at Noshiro (Cases 07 and 08), the wind speed and direction were vertically and logarithmically interpolated to match the objective heights.

Case	Site	Reference Point	Target Point	Height at Reference and Target Point [m AMSL]	Distance Between Reference and Target Point [m]	Distance Between Shoreline and Target Point [m]	# of Sample
01 02 03	Mutsu-Ogawara	St. A *	St. B	50 120 200	1604	1040	45,157
04 05 06	Sakata	LL *	BL	53 113 173	3374	1380	18,119
07	Noshiro	CMT	SL *	57	4065	2750	28,098
08			VL *	57	4290	520	
09 10 11 12 13 14	Yuri-Honjo	SVL	SSL NSL 	40 100 160 40 100 160	2115 11,890 	1750 2040 	29,955

Figure 2a illustrates the two measurement points surrounding the Mutsu-Ogawara port in Aomori Prefecture. The coastline runs north–south, with the Pacific Ocean to the east and hilly terrain to the west. Vertical LiDARs (VL; Windcube v2, manufactured by Vaisala, headquartered in Vantaa, Finland) [21] were installed at two locations: one on the western land side (St. A) and one on the breakwater (St. B). St. A, situated on a sandy beach, was used as the reference point, while St. B, surrounded by open water, was treated as an offshore point in this study. The distance between stations A and B is 1604 m. Regarding data filtering at the two vertical LiDARs, it was performed based on the quality control flags output by the LiDAR system. The verification period was one year, from 1 January to 31 December 2021, Japan Standard Time (JST).

Figure 2b shows two measurement points located in or near Sakata City, Yamagata Prefecture, Japan. The coastline runs from north-northeast to south-southwest, with the Sea of Japan to the west and flat plains to the east. Vertical LiDAR (DIABREZZA, manufucrured by Mitsubishi Electric Corporation, headquartered in Tokyo, Japan) [22] was installed at points on the northern land side (LiDAR-on-land point; LL) and the southern offshore side (BuoyLiDAR point; BL). LL was located on a sandy beach along the coastline, with a coastal windbreak forest situated on the landward side and BL, mounted on a floating buoy, was situated at an offshore point. LL was used as the reference point and BL was used as the target point. The distance between the LL and BL was 3374 m. Regarding data filtering at the two vertical LiDARs, it was performed based on the quality control flags output by the LiDAR system. The verification period was approximately five months, from 12:00 on 9 July 2018 to 00:00 on 13 December 2018, Japan Standard Time (JST).

Figure 2c depicts the three measurement points near Noshiro Port in the northern part of Akita Prefecture. The coastline runs approximately north–south, with plains spreading inland to the east. A meteorological mast was built in the central part of this site (referred to as CMT), and the highest cup anemometer data were used in this study. The mast was located on a sandy beach along the coastline, with a coastal windbreak forest situated on the landward side. A vertical LiDAR (ZX300M, manufactured by ZX Lidars, headquartered in Ledbury, United Kingdom) [23] was installed on the breakwater (VL). VL, surrounded by open water, was treated as an offshore point in this study. Regarding data filtering at the vertical LiDAR, it was performed based on the quality control flags output by the LiDAR system. The other offshore point (SL) was measured using two scanning LiDARs (Windcube 200S, manufactured by Vaisala, headquartered in Vantaa, Finland) installed on land, forming a dual-scanning LiDAR system (DSL). This point was also treated as an offshore point in this study. In this DSL measurement, the horizontal wind vectors were reconstituted from two line-of-sight (LOS) wind speeds based on a previous study [24]. Specifically, the measurements by RHI scans were obtained at three heights, with 18 samples per height acquired over each 1 min interval. After reconstruction, outliers exceeding $\pm 3\sigma$ from the mean were removed, and 10 min averages of wind speed and direction were subsequently calculated. The CMT was used as the reference point, and the VL and SL were used as target points. The CMT was located 4065 m and 4290 m from the SL and VL, respectively. The period for verification was one year, from 1 August 2020, to 31 July 2021, JST.

Figure 2d shows the four measurement points located in and near Yuri-Honjo City in the southern part of Akita Prefecture. The coastline also runs approximately north–south, with hilly terrain inland to the east. A narrow plain area is located in the southern part. The measurement equipment for the vertical LiDAR (ZX 300M) and scanning LiDAR (streamline XR) were installed at an onshore point near the coastline on the south side (SVL), and the measurement equipment for the scanning LiDAR (streamline XR, manufactured by Lumibird, Lannion, France) was installed at another onshore point near the coastline on the

north side. The vertical LiDAR at the SVL measured the wind at the installation point. SVL was located on a sandy beach along the coastline, with a coastal windbreak forest situated on the landward side. Regarding data filtering at SVL, it was performed based on the quality control flags output by the LiDAR system. Single-scanning LiDARs at NVL and SVL measured the wind at the NSL and SSL points (2 km offshore), respectively. These points were treated as an offshore point in this study. Horizontal wind vector measurements with single-scanning LiDAR were performed using the single-LOS reconstitution method described in a previous study [25]. Specifically, the measurements by PPI scans were obtained at three heights, with 12 samples per height acquired over each 10 min interval (i.e., one sample every 15 s per height). After removing line-of-sight (LoS) data based on SNR values and performing reconstruction, 10 min averages of wind speed and direction were calculated. Only timestamps in which at least 7 samples were obtained at a given height within each 10 min period were used in the analysis. This study used data from these three points (SVL, NSL, and SSL); SVL was used as the reference point, and NSL and SSL were used as the target points. The distances from the SVL to the SSL and NSL were 2115 and 11,890 m, respectively. The period for verification was one year, from 1 February 2020, to 31 January 2021, JST.

This study used a 10 min mean wind speed and direction, restricting the dataset to timestamps that were valid at all points and heights used for verification at each site to ensure comparability among cases within the same site. It is noted that, for St. A at Mutsu-Ogawara (Case 01–03), LL at Sakata (Case04–06), and SL and VL at Noshiro (Cases 07 and 08), the wind speed and direction were vertically interpolated using the logarithmic wind profile to match the objective heights.

2.2. Model and Methods to Estimate Time Series

This section provides an overview of the five estimation methods for wind speed and direction verified in this study.

Table 3 shows an overview of the five methods.

Table 3. Five estimation methods.

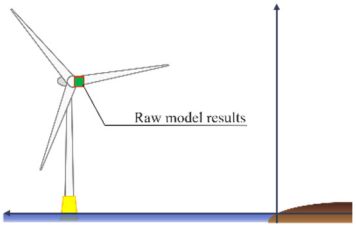
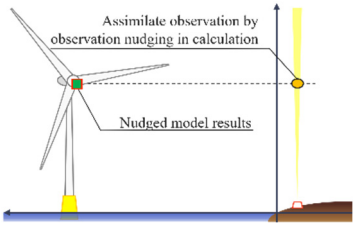
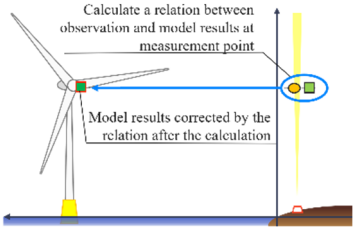
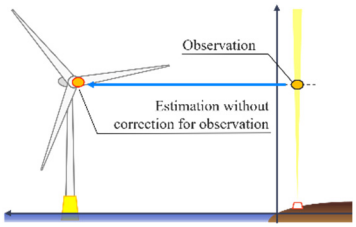
Abbreviation	Method	Material		Schematic
		Measurement	Model Results	
CTRL	WRF control simulation without on-site measurement data		✓	
NDG	Online method	Observation nudging	✓	✓	

Table 3. *Cont.*

Abbreviation	Method		Material		Schematic
			Measurement	Model Results	
TC	Offline method	Temporal correction method	✓	✓	
DE		Directional extrapolation method	✓	✓	
DA	Directly Apply a time series at reference point		✓		

(a) WRF control simulation without on-site measurement data (CTRL)

The first estimation method was a control simulation using a mesoscale meteorological model without onsite measurement data (CTRL). In this study, WRF (version 3.8.1/4.1.2) was used as a mesoscale meteorological model. WRF is a non-hydrostatic and fully compressible model that is commonly used in wind condition surveys of wind energy. Table 4 presents the configurations of WRF used in this study, which are common for methods (b)–(d) described below. This configuration is based on the NeoWins Project and related studies [6,16,26]. The continuous calculation period was half a month (17 days at most), including the span of the spin-up, which was 1 day. The differences between the previous project and this study are that the surface roughness [26], the calculation period (monthly to half-monthly), and the input of the meteorological (JMA ((Japan Meteorological Agency)-MANAL (Meso Analysis) to JMA-LFM (Local Forecast Model)) and sea surface temperature data (MOSST (MODIS-based Sea Surface Temperature) to OSTIA (Operational Sea Surface Temperature and Sea Ice Analysis)) were adjusted. As shown in Figure 3, the model domains were set for each objective site. The horizontal grid spacing was refined from 2.5 to 0.1 km resolution by a factor of five through two nested domains.

Table 4. Common configuration of all calculations by WRF.

Model Version	WRF (ARW: Advanced Research WRF) V3.8.1 (Noshiro, Yuri-Honjo)/4.1.2(Sakata, Mutsu-Ogawara)	
Input data	Met	JMA-LFM (1 hourly, 0.02° × 0.025°)
	Soil	NCEP FNL (National Centers for Environmental Prediction Final Operational Global Analysis) (6 hourly, 1° × 1°)
	SST	Met Office OSTIA (Daily, 0.05° × 0.05°)
Terrain data	Elevation	METI (Ministry of Economy, Trade and Industry (Japan)), NASA (National Aeronautics and Space Administration), ASTER-GDEM (Advanced Spaceborne Thermal Emission and Reflection Radiometer Global Digital Elevation Model)
	Land use	MEIT, MLNI (Ministry of Land, Infrastructure, Transport and Tourism (Japan)) land use subdivision mesh
	Roughness Table	Based on JMA but Mixed Forest (3.0 m by JMA) is 2.0 m in only Noshiro and Yuri-Honjo
Grid spacing	d01	2.5 km
	d02	0.5 km
	d03	0.1 km

Table 4. *Cont.*

Model Version		**WRF (ARW: Advanced Research WRF) V3.8.1 (Noshiro, Yuri-Honjo)/4.1.2(Sakata, Mutsu-Ogawara)**
Vertical levels		40 layers (Surface to 100 hPa)
Physics options	Shortwave	Dudhia scheme
	Longwave	Rapid Radiative Transfer Model scheme
	Microphysics	Ferrier (new Eta) scheme
	Planetary Boundary Layer	Mellor-Yamada-Janic (Eta operational) scheme
	Surface layer	Monin-Obukhov (Janic Eta) scheme
	Land surface	Noah Land Surface Model scheme
	Cumulus Parameterization	Kain-Fritsch (new Eta) scheme (only d01)
FDDA	d01	Enabled (u, v, θ, q)
	d02, d03	Enabled (u, v, θ, q) above the thirteen layers (about 2 km)

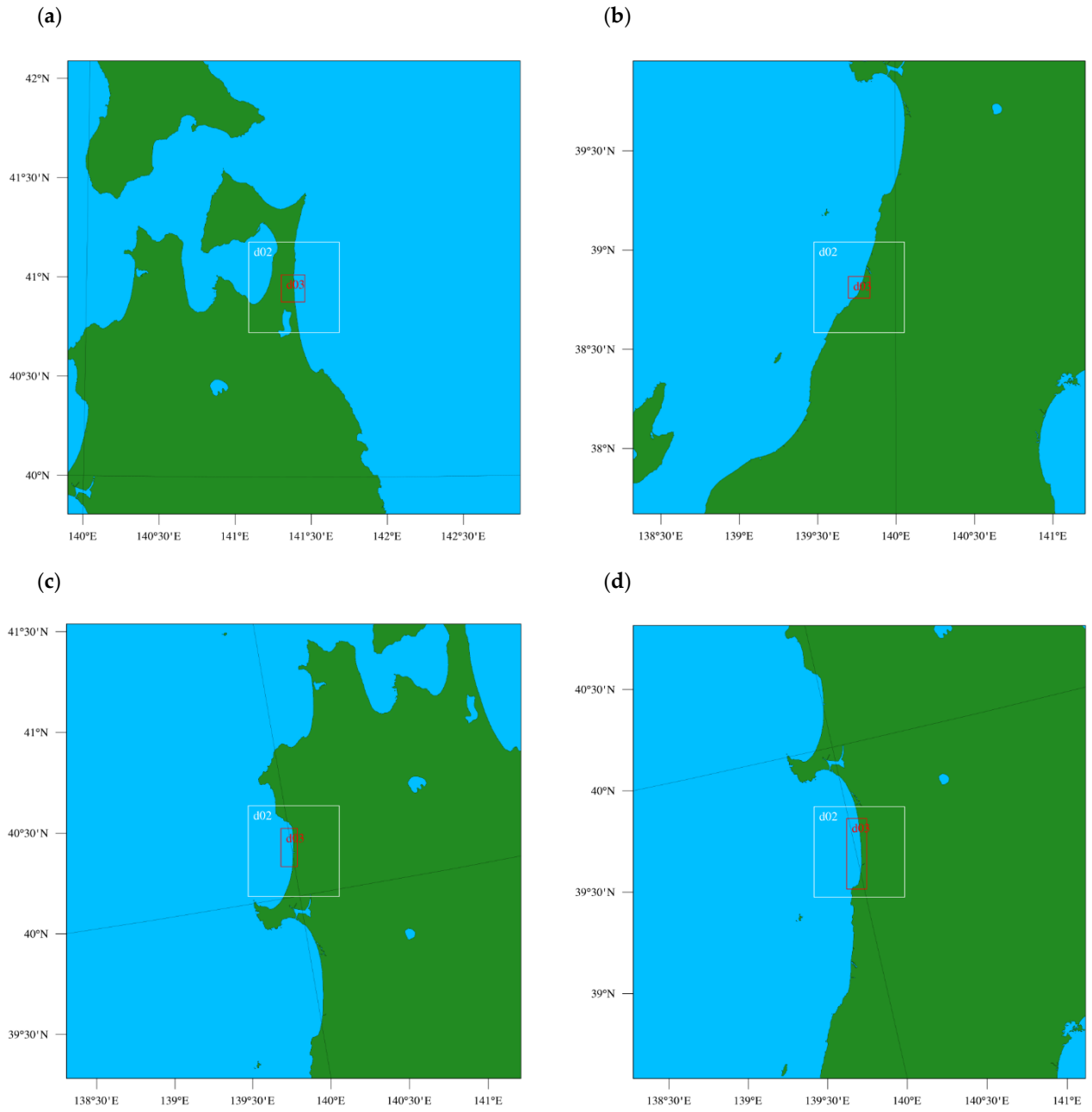


Figure 3. Simulation domains by WRF: (**a**) Mutsu-Ogawara, (**b**) Sakata, (**c**) Noshiro, and (**d**) Yuri-Honjo. The entire figure is d01, the site surrounded by white lines is d02, and the site surrounded by red lines is d03.

Table 5 shows the calculation period and number of calculation grids.

Table 5. Unique configuration of each calculation by WRF.

Site	Period (Not Including the Spin-Up Period)		Grid d01	Grid d02	Grid d03
Mutsu-Ogawara	1 January 2021–31 December 2021	(1 year)	100 × 100	100 × 100	130 × 150
Sakata	1 July 2018–31 December 2018	(6 months)	100 × 100	100 × 100	120 × 120
Noshiro	1 August 2020–31 July 2021	(1 year)	100 × 100	100 × 100	90 × 210
Yuri-Honjo	1 February 2020–31 January 2021	(1 year)	100 × 100	100 × 100	110 × 390

The time series of CTRL was created by extracting the wind speed and direction at the target point and height by spatially interpolating the grid point data from the results simulated by WRF. Specifically, the four grid points surrounding the target point are logarithmically interpolated to the target height and bilinearly interpolated to the target point.

(b) Online method: observation nudging (NDG)

The second method integrates onsite measurement data into a WRF simulation using observation nudging (NDG). Observation nudging is one of the simplest data assimilation methods for improving the background field or first guess. One FDDA option was implemented within WRF [17,18]. It has been used for improving weather forecasting accuracy and for reanalysis purposes. In this study, observation nudging is called an "online method" as it entails correcting calculated values "On the Line" of a calculation.

In the observation nudging process, the model is locally forced toward the corresponding observation at each time step using an additional tendency term as follows:

$$\frac{\partial a\mu_d}{\partial t}(x,y,z,t) = F_a(x,y,z,t) + \mu_d G_a \frac{\sum_{i=1}^{N} W_a^2(i,x,y,z,t)[a_0(i) - a_m(x_i,y_i,z_i,t)]}{\sum_{i=1}^{N} W_a(i,x,y,z,t)} \quad (1)$$

where a represents the quantity being nudged (u and v are wind components in this study); μ_d represents the mass of the dry air in the column; F_a represents the physical tendency terms for a; G_a represents the nudging strength for a; N represents the total number of observations; i represents the index to the current observation; and W_a represents the spatiotemporal weighting function based on the settings of nudging coefficient, horizontal and vertical radii, and time window.

The observation nudging configurations used in this study are presented in Table 6. Regarding the nudging coefficient, which is typically set to range from 10^{-4} to 10^{-3} to avoid degrading internal mesoscale variability in the model [27], the authors considered using a default value of 0.6×10^{-3} and a larger nudging coefficient than the final value of 1.2×10^{-3} used in this verification; however, the default value nudged less effectively than 1.2×10^{-3}, and in certain cases, the calculation diverged when the value exceeded 1.2×10^{-3}; therefore, the authors adopted 1.2×10^{-3}, which can be computed stably.

Table 6. Common configuration of the observation nudging method.

Variable	Setting
Valid domain	d03
Input (Reference) data	u- and v-components converted from 10 min horizontal mean wind speed and direction
Nudging coefficient	1.2×10^{-3}
Horizontal radius of influence	20 km
Half-period time window	6 min 40 s

Table 7 presents the measurements used as input and the vertical radius of influence of the nudge in the simulation for each site. The process for extracting simulation results is the same as that for CTRL. The vertical radius of influence was approximately equal to the measurement interval if the input was multi-height; otherwise, it was approximately 60 m. All non-missing measurements were used as input data for this method.

Table 7. Unique configuration of the observation nudging method in each site.

Case	Site	Reference Point (Its Height [m AMSL])	Vertical Radius of Influence [m] (Convert Sigma Levels Grid into Meter)
01–03	Mutsu-Ogawara	St. A (50, 66, 87, 107, . . ., 207)	About 20
04–06	Sakata	LL (51.5, 71.5, . . ., 211.5)	About 20
07–08	Noshiro	CMT (57)	About 60
09–14	Yuri-Honjo	SVL (40, 100, 160)	About 60

(c) Offline method: Temporal Correction method (TC)

Methods (c) and (d) estimated the wind conditions at the target point using the relationship between the measurement data and WRF-simulated results at the reference point after completing the WRF calculation. In this study, these methods are called the "offline method" in contrast with the "online method." This study examines two dominant offline methods.

The first offline method is the temporal correction (TC) method. This method can be regarded as "correction" of wind vector error between the measurement data and the WRF-simulated result at the reference point for each timestamp. This method allows for incorporating the temporal evolution of both the WRF's spatial structure and its simulation errors. The formulae for TC (Figure 4) are as follows:

$$\boldsymbol{V}_{tgt}^{EST}(x,\ y,\ z,\ t) = \boldsymbol{V}_{tgt}^{WRF}(x,\ y,\ z,\ t) + \boldsymbol{\epsilon_{ref}}\left(x_{ref},\ y_{ref},\ z_{ref},\ t\right) \tag{2}$$

$$\boldsymbol{\epsilon_{ref}}\left(x_{ref},\ y_{ref},\ z_{ref},\ t\right) = \alpha\ \Delta\boldsymbol{V_{ref}}\left(x_{ref},\ y_{ref},\ z_{ref},\ t\right) = \alpha\ \left(\boldsymbol{V}_{ref}^{OBS}\left(x_{ref},\ y_{ref},\ z_{ref},\ t\right) - \boldsymbol{V}_{ref}^{WRF}\left(x_{ref},\ y_{ref},\ z_{ref},\ t\right)\right) \tag{3}$$

where $\boldsymbol{V}$ represents the horizontal wind vector (10 min values in this study); $x,\ y,\ z$ represents the coordinate point of a target point; $x_{ref},\ y_{ref},\ z_{ref}$ represents the coordinate point of a reference point; t represents a timestamp; $\boldsymbol{V}_{tgt}^{EST}$ represents the estimation result at the target point; $\boldsymbol{V}_{tgt}^{WRF}$ represents the model result at the target point; $\boldsymbol{\epsilon_{ref}}$ represents the correction term; α is the weighting coefficient; and $\Delta\boldsymbol{V_{ref}}$ represents the error vector between the observation $\boldsymbol{V}_{ref}^{OBS}$ and model result $\boldsymbol{V}_{ref}^{WRF}$ at the reference point. Although the weighting function α should ideally be a function of spatial variables, its functional form has not yet been well established owing to a lack of sufficient empirical validation. Therefore, in this study, α was set to 1. This implies that the wind vector error is assumed to be spatially homogeneous over the objective site. TC can estimate wind direction as well

as wind speed, as it considers two components of wind speed. Notably, TC corresponds to implementing observation nudging after the completion of the WRF calculation.

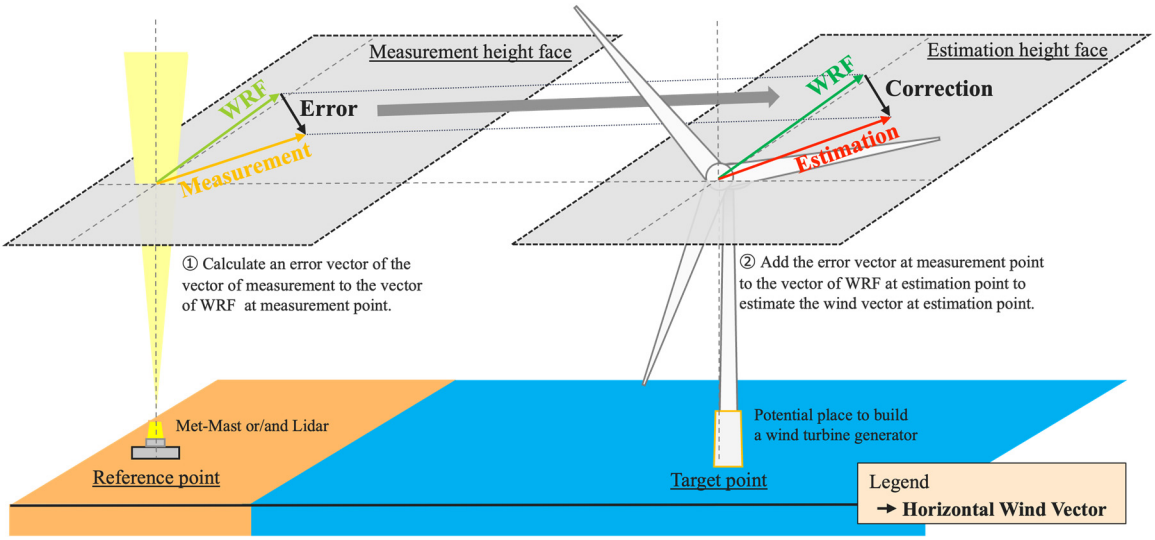


Figure 4. Schematic illustrating TC application.

In this method, the reference height at the reference point and the target height at the target point were set to the same value.

(d) Offline method: directional extrapolation method (DE)

The second method involves the use of an offline method to apply feature values for each wind direction. This method is generally used to spatially extrapolate CFD. The authors examined the formulae shown in a previous study [28,29] as follows:

$$U_{tgt}^{EST}(x,\ y,\ z) = U_{ref}^{OBS} \cdot C_U^{WRF}\left(x,\ y,\ z,\ \theta_{ref}^{OBS}\right) \tag{4}$$

$$C_U^{WRF}(x,\ y,\ z,\ n) = \frac{U_{tgt}^{WRF}(x,\ y,\ z,\ n)}{U_{ref}^{WRF}\left(x_{ref},\ y_{ref},\ z_{ref},\ n\right)} \tag{5}$$

$$C_U^{WRF}\left(\theta_{ref}^{OBS}\right) = C_U^{WRF}(n) + a\ \left(\ C_U^{WRF}(n+1) - C_U^{WRF}(n)\right) \tag{6}$$

$$\theta_{tgt}^{EST}(x,\ y,\ z) = \theta_{ref}^{OBS} + \Delta\theta^{WRF}\left(x,\ y,\ z,\ \theta_{ref}^{OBS}\right) \tag{7}$$

$$\Delta\theta^{WRF}(x,\ y,\ z,\ n) = \theta_{tgt}^{WRF}(x,\ y,\ z,\ n) - \theta_{ref}^{WRF}\left(x_{ref},\ y_{ref},\ z_{ref},\ n\right) \tag{8}$$

$$\Delta\theta^{WRF}\left(\theta_{ref}^{OBS}\right) = \Delta\theta^{WRF}(n) + a\ \left(\ \Delta\theta^{WRF}(n+1) - \Delta\theta^{WRF}(n)\right) \tag{9}$$

$$a = \frac{\theta_{ref}^{OBS} - \theta_{ref}^{WRF}(n)}{\theta_{ref}^{WRF}(n+1) - \theta_{ref}^{WRF}(n)} \tag{10}$$

$$\theta_{ref}^{OBS} \in \left(\theta_{ref}^{WRF}(n),\ \theta_{ref}^{WRF}(n+1)\right) \tag{11}$$

where U represents wind speed, θ represents wind direction, C_U^{WRF} and $\Delta\theta^{WRF}$ represent the wind speed ratio and the change in wind direction between the target and reference points, respectively, and $n\ (=0-15)$ and $n+1$ denote the two adjacent wind sectors determined by the measured wind direction at the reference point. Each index n corresponds to a specific wind direction: 0 or 16 represents 0° (N), 1 represents 22.5° (NNE), and 15 represents 337.5° (NNW). a represents a proportional coefficient for linear interpolation

to C_U^{WRF} and $\Delta\theta^{WRF}$ between two adjacent wind direction sectors of wind direction at reference point, and the subscripts are the same as those in Formulas (2) and (3). This method can be interpreted as the multiplication of the wind speed ratio and the addition of the wind direction, both defined between the target point and the reference point based on the model results, and applied as a scale and offset to the measurement data at the reference point.

In this method, the reference height at the reference point and the target height at the target point were set to the same height as in method (c), TC.

(e) Direct-application method (DA)

The fifth method is the direct use of the measurement data of the reference point as estimates of the target point without any correction. This approach implicitly assumes that the wind conditions at the reference and target points are identical, without accounting for any spatial heterogeneity between the points. In this method, the reference height at the reference point and the target height at the target point were set to the same height. Even though this method is not practically used, a comparison of the accuracy of this method and those involving the other four methods which use model results can be used to demonstrate the effectiveness of "spatial extrapolation" by WRF.

2.3. Evaluation Parameters

2.3.1. General Key Performance Indicators (KPIs)

In this section, the authors describe the statistical verification indicators used in this study. First, the authors defined the model error as described in a previous study [7].

$$e(t) = P(t) - O(t) \tag{12}$$

where $P(t)$ is the estimation and $O(t)$ is the measurement for each timestamp, t.

The bias (mean error) was the average of each timestamp error between the estimated and true values, and the relative bias was the bias divided by the mean of the true values.

$$Bias = \frac{1}{n}\sum_{i=1}^{n} e_i \tag{13}$$

$$Relative\ Bias\ [\%] = \frac{Bias}{\frac{1}{n}\sum_{i=1}^{n} O_i} \times 100 \tag{14}$$

where e_i is the error between the estimation and measurement at the target point and n is the sample size.

The root mean square error (RMSE) and relative RMSE have been widely used to evaluate the accuracy of model reproducibility in meteorology [30]. The RMSE is expressed as follows:

$$RMSE = \sqrt{\frac{1}{n}\sum_{i=1}^{n} e_i^2} \tag{15}$$

$$Relative\ RMSE\ [\%] = \frac{RMSE}{\frac{1}{n}\sum_{i=1}^{n} O_i} \times 100 \tag{16}$$

Carbon Trust Offshore Wind Accelerators (OWA) provide key performance indicators (KPIs) to assess the maturity of floating LiDARs and the substitutability of offshore meteorological masts [31]. This study also evaluated KPIs. The wind speed KPIs are the slope and coefficient of determination of a single-variant regression, with the regression analysis

constrained to pass through the origin ($y = mx + b;\ b = 0$). The slope a and coefficient of determination R^2 [32] are expressed as follows:

$$a = \frac{\sum x_i y_i}{\sum x_i^2} \tag{17}$$

$$R^2 = 1 - \frac{\sum (y_i - \hat{y}_i)^2}{\sum (y_i - \overline{y})^2} \tag{18}$$

where x_i is an independent variable, y_i is a dependent variable, $\hat{y}_i$ is an estimate using regression, and $\overline{y}$ is the mean value of y_i.

The wind direction KPIs are the slope and coefficient of determination of a single-variant regression with an intercept ($y = mx + b$). The slope a and intercept b are expressed as follows:

$$a = \frac{\Sigma (x_i - \overline{x})(y_i - \overline{y})}{\Sigma\ (x_i - \overline{x})^2} \tag{19}$$

$$b = \overline{y} - a\overline{x} \tag{20}$$

The coefficient of determination R^2 is expressed in Equation (18).

Additional processing was applied to the wind direction when the indicators were applied. This is because the absolute value of the error between the estimation and measurement for verification can exceed 180°. If the error between the estimation and measurement at a certain time was 180° or more, the estimation was subtracted by 360°; conversely, if the error was less than −180°, the estimation was added to 360° and then each indicator was calculated.

The combination of bias, slope, and intercept of the regression line, as well as the combination of RMSE and R^2, represents statistical indicators with similar characteristics within their respective combinations. However, because these indicators are commonly used, all of them were adopted in this study.

2.3.2. Wind Speed Difference Between Reference and Target Points

The role of the wind flow model is spatial extrapolation, or more specifically, accurate estimation of the wind field between a reference point and the target point. Hence, owing to the importance of evaluating the relationship between the average wind speeds at a reference point and the target point in the accuracy assessment, the wind speed ratio γ and wind speed difference δ between a reference point and the target point are expressed as follows;

$$\gamma = \frac{U_{tgt}}{U_{ref}} \tag{21}$$

$$\delta = U_{tgt} - U_{ref} \tag{22}$$

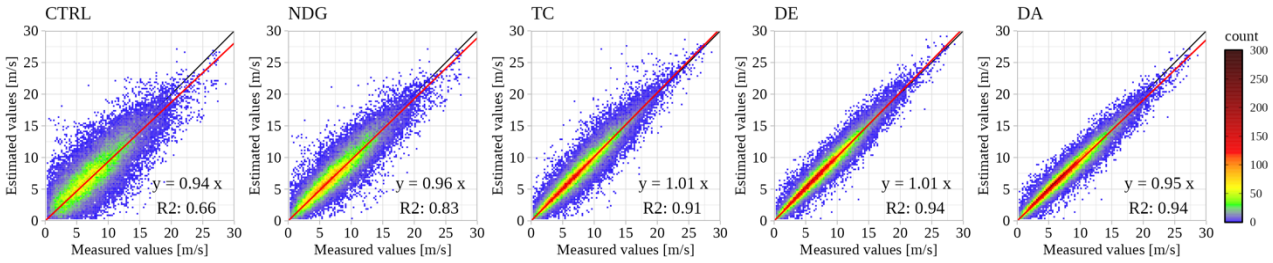
The reason for comparing both the wind speed ratio γ and the wind speed difference δ is to avoid an evaluation strongly dependent on the characteristics of the method. Specifically, the wind speed ratio between the reference and target points appears in the DE formula, whereas the vector difference in the wind speed between the reference and target points appears in the NDG and TC formulas.

3. Results

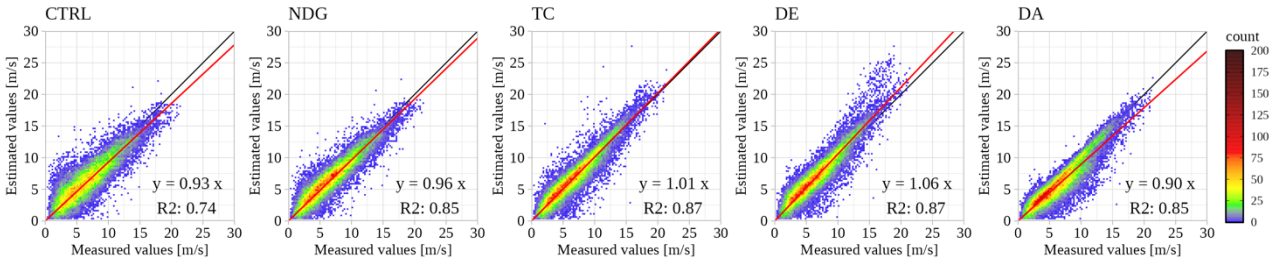
In this study, the measured data at the target (or reference) points were used as true values, whereas the estimated values from the five methods served as validation values. Figure 5 presents density scatter plots comparing the measured wind speeds and wind speeds estimated by the five methods at St. B (Mutsu-Ogawara), SL (Noshiro), and NSL

(Yuri-Honjo). This figure is included for illustrative purposes and to aid in the interpretation of the KPIs used in the evaluation.

Case 02 Mutsu-Ogawara 120 m



Case 07 Noshiro SL 57 m



Case 13 Yuri-Honjo NSL 100 m

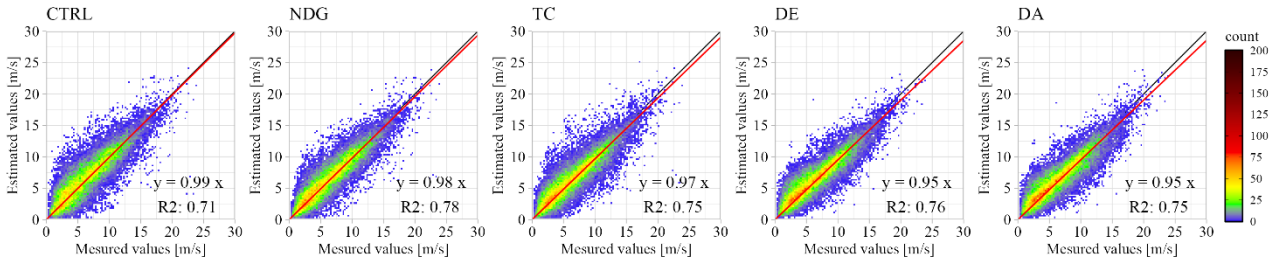


Figure 5. Scatter density plots of estimated values versus true values (measured) for each method. The vertical axis represents the estimated values, the horizontal axis represents the measured values, the colors indicate scatter density, the red lines indicate single regression lines without the intercept and the black lines indicate $y = x$.

This section presents the results of the evaluation of the time series of wind speed and wind direction at 14 target points at four sites, as introduced in Section 2.1, using the five methods described in Section 2.2, based on the KPIs outlined in Section 2.3. Tables A1 and A2 in Appendix A provide all KPIs for each method at the 14 target points introduced in Section 2.3.1. Section 3.1 presents an analysis of the statistical properties. In Section 3.2, the relationship between one of the KPIs, the bias, and the differences in wind speed between the reference and target points were examined, and in Section 3.3, the KPIs, considering the characteristics of each site, were analyzed.

3.1. KPIs of Estimation Time Series by Five Estimation Methods

This section shows the KPIs of the five methods described in Section 2.2 to evaluate their accuracy. Figure 6; Figure 7 show the average values and their variation as statistical results of the accuracy indicators for wind speed and wind direction, respectively.

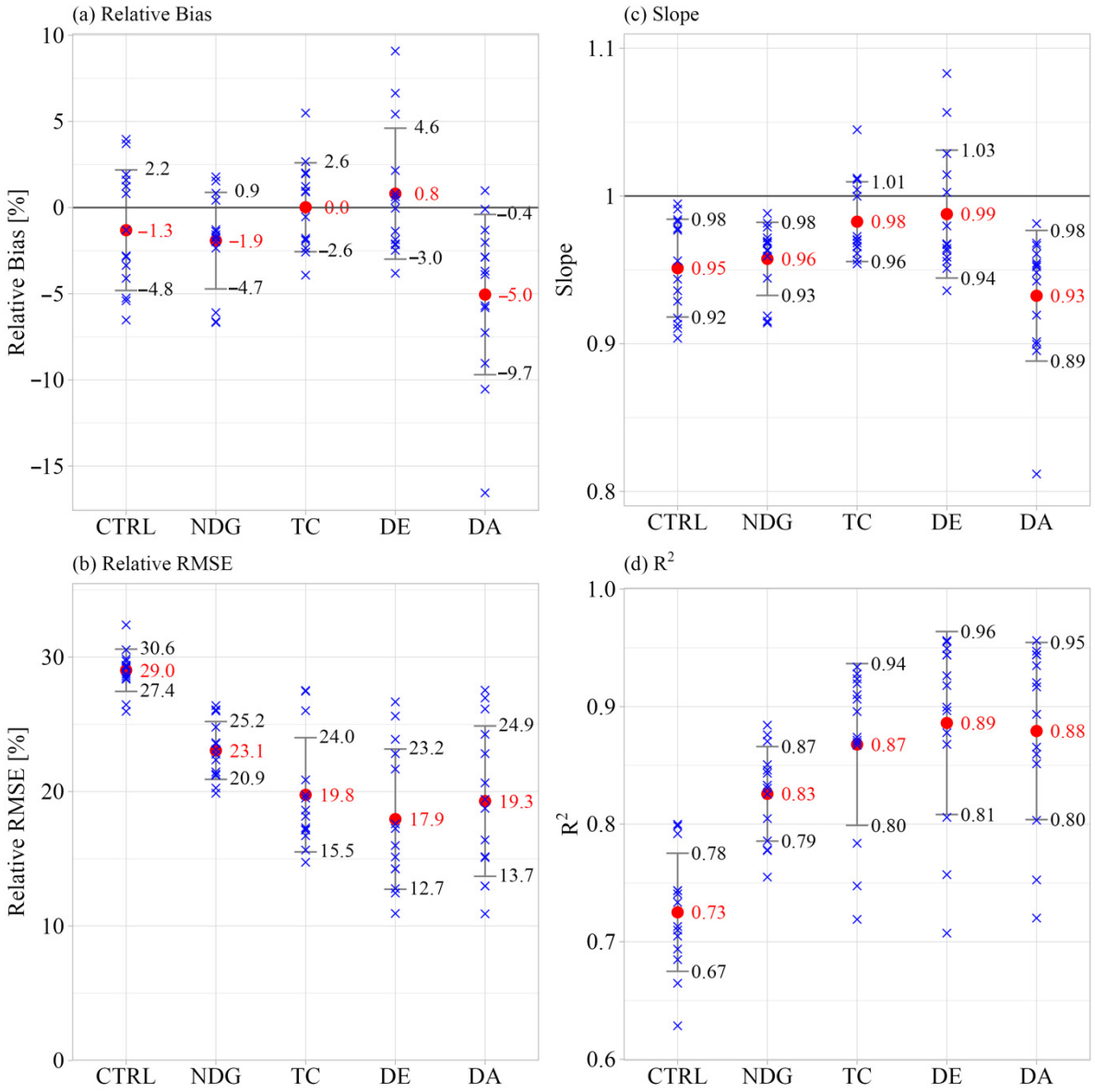


Figure 6. Statistics of (**a**) relative bias, (**b**) relative RMSE, (**c**) slope, and (**d**) R^2 for wind speed estimates compared to the true values at four sites. The vertical axis represents each statistic, and the horizontal axis indicates the estimation methods. Each blue plot shows individual cases, the red points indicate the mean, and error bars represent the range of $\mu \pm 1.28\sigma$.

First, the statistical values of wind speed bias are shown in Figure 6a. CTRL, which uses only WRF, had a mean value of −1.3% and a standard deviation of 3.5%. In contrast, DA, which uses only measurement data, had a mean value of −5.0% and standard deviation of 4.6%. The relatively large negative mean value indicated that the average wind speed at the offshore target points was higher than the average wind speed at the reference points near the coastline. In coastal sites, accurately estimating the difference in the average wind speed is essential. Subsequently, CTRL was compared with three estimation methods (NDG, TC, and DE) that used both the measurement data and WRF. For CTRL and NDG, the mean values were −1.3% for CTRL and −1.9% for NDG, with CTRL being closer to 0. However, the standard deviation of NDG (2.8%) was smaller than that of CTRL (3.5%). For CTRL and TC, TC had a mean value (0.0%) closer to 0 and a smaller standard deviation (2.6%) compared to CTRL. For CTRL and DE, the mean value of DE (0.8%) was closer to zero, but the standard deviation (3.8%) was relatively large. Therefore, TC showed the

smallest mean bias and standard deviation, suggesting that it had the highest probability of approaching 0% bias.

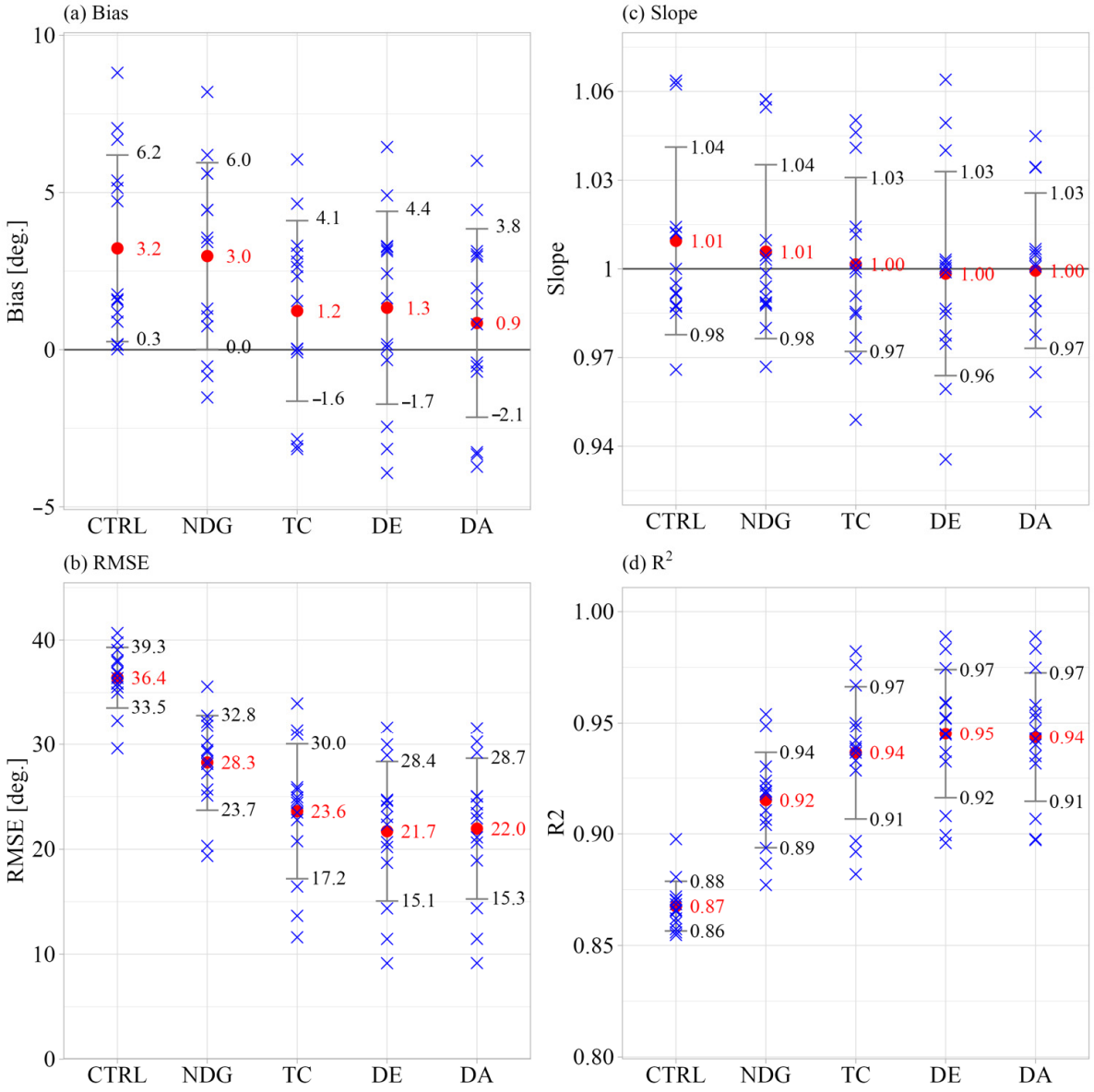


Figure 7. Statistics of (**a**) bias, (**b**) RMSE, (**c**) slope, and (**d**) R^2 for wind direction estimates compared to the true values at four sites. The vertical axis represents each statistic, and the horizontal axis indicates the estimation methods. Each blue plot shows individual cases, red plots indicate the mean, and error bars represent the range of $\mu \pm 1.28\sigma$.

Second, the statistical values of the slope of the regression line of the wind speed are shown in Figure 6c. All methods tended to underestimate the slope, but the relative relationship between the methods showed a trend similar to that of the bias. In terms of the mean, DE was closest to 1; however, considering its variation, TC had the highest probability of approaching 1.

Third, the statistical values of the coefficient of determination (R^2) for the wind speed regression line are shown in Figure 6d. CTRL had a mean value of 0.73 and a standard deviation of 0.05, while DA had a mean value of 0.88 and a standard deviation of 0.08. Although CTRL is the WRF calculation result at the target points and DA is the measurement data at the reference points, DA clearly had higher values, indicating that the temporal variation at the reference points was closer to the measurement data at the target points

than the temporal variation from WRF. Subsequently, CTRL and DA were compared to three other methods (NDG, TC, and DE). The mean R^2 values for these methods were significantly higher than those for CTRL, demonstrating their effectiveness in improving the reproducibility of time series when incorporating measurement data. NDG had lower values than DA, whereas TC and DE were comparable to DA. Comparing the three methods (NDG, TC, DE), the mean R^2 values were in the order of DE (0.89), TC (0.87), and NDG (0.83), while the standard deviations were in the order of NDG (0.04), TC (0.07), and DE (0.08). Although DE had the largest mean R^2 value, it also had the largest standard deviation. Conversely, NDG had the smallest mean R^2 value and standard deviation. TC fell between NDG and DE, but its values were closer to DE than NDG. Therefore, DE and TC captured temporal variations relatively accurately in the three methods.

Fourth, the statistical values of the RMSE of wind speed are shown in Figure 6b. Regarding the RMSE, the relative relationship between the methods followed a trend similar to that of the R^2, with DE having the smallest mean value.

The KPIs for wind direction are shown in Figure 7. The wind direction bias was small across all methods, with mean values ranging from 0.9° to 3.2°, suggesting that its impact on the practical estimation accuracy of power generation was negligible, regardless of the method used. However, DA had the smallest mean bias, closest to 0 at 0.9°, and a mean coefficient of determination of 0.94, comparable to those of TC and DE. This indicates that for the sites used in this analysis, the difference in wind direction between a reference point and the target point was small and did not significantly affect the estimation accuracy.

In this section, the KPIs for the wind speed and wind direction are compared across the five methods. For wind speed bias, TC demonstrated the best results, showing the smallest bias and standard deviation. Additionally, in terms of the coefficient of determination (R^2), TC and DE exhibited high values, capturing temporal variations relatively accurately. DA exhibited the highest accuracy for wind direction estimation; however, the other methods also achieved an accuracy level within the range required for practical applications.

3.2. Accuracy of Wind Speed Difference Between Reference and Target Points

In the previous section, the estimation accuracies at the target points were discussed. However, in actual wind condition estimations, the spatial distribution of the wind conditions needs to be reproduced. Therefore, it is important to accurately reproduce not only the wind speed at the target points but also the wind speed at the reference points and the horizontal wind speed relationship between a reference point and the target point.

First, Figure 8 shows the relative wind speed (referred to here as "relative wind speed" for convenience), calculated by subtracting the average wind speed of the reference point's measurement data from the average wind speed estimated by each of the five methods for both a reference point and the target point. The horizontal axis represents the reference and target points and the vertical axis represents the relative wind speed. CTRL and NDG had relative wind speeds that were not 0 m/s at the reference point, whereas TC and DE had relative wind speeds that were 0 m/s at the reference point. These differences reflected the characteristics of each method. In other words, when interpreting the bias at the target point, the biases of CTRL and NDG were composed of two elements: the bias at the reference point and the reproducibility of the horizontal wind speed difference, whereas the biases of TC and DE were composed of only the latter. The KPIs of CTRL and NDG at the reference points are presented in Tables A3 and A4 in Appendix A.

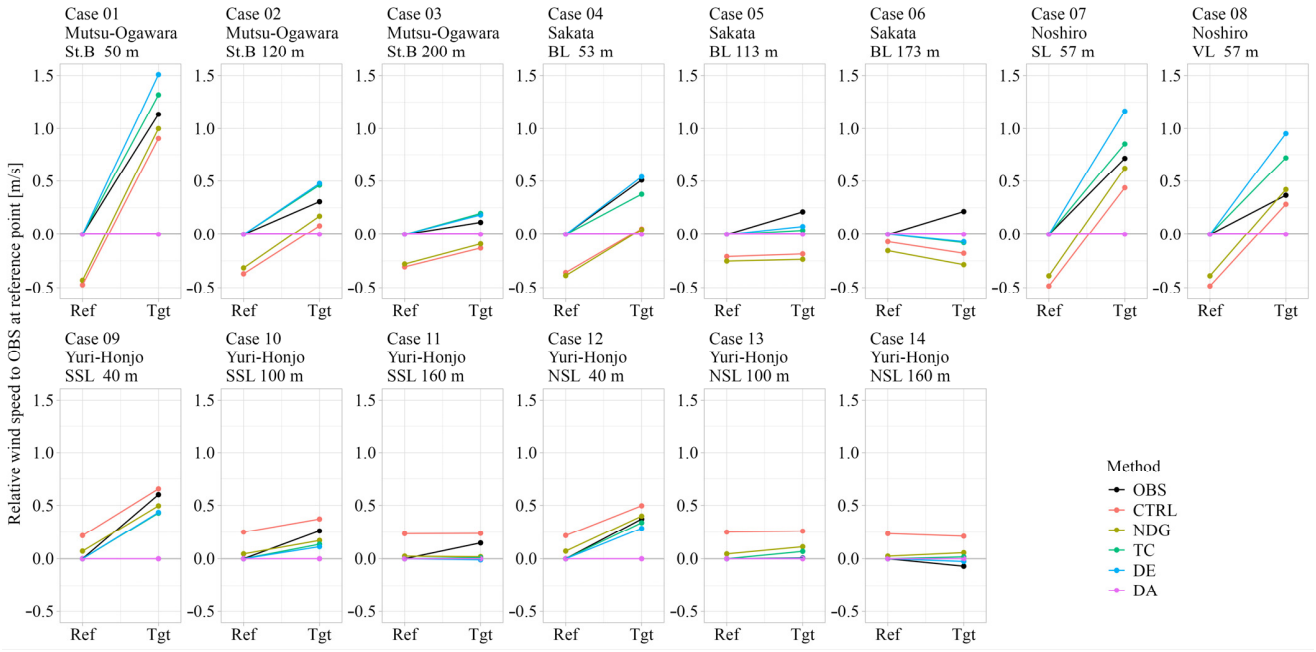


Figure 8. Variation in the relative mean wind speed of each estimation method at the reference and target points relative to the measured mean wind speed at the reference point. The horizontal axis represents the reference point (Ref) and the target point (Tgt), the vertical axis represents the relative mean wind speed of each estimation method between the reference point and the target point relative to the measured mean wind speed at the reference point, the colors indicate the estimation methods, and each figure corresponds to a specific estimation site and its height—a case.

Second, the results of the accuracy verification for the differences and ratios of the average wind speeds between the reference and target points using the indicators described in Section 2.3.2 are presented. Figure 9 shows the scatter plots of the horizontal wind speed differences and ratios, with measured values and those estimated using the four methods (excluding DA).

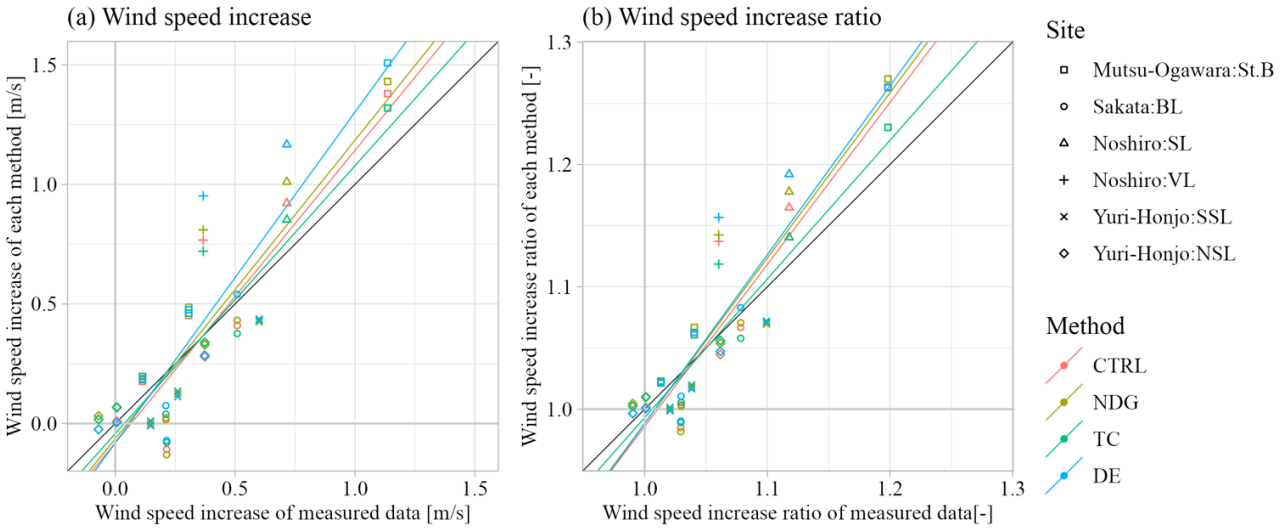


Figure 9. Scatter plot and single regression line of wind speed difference estimated by each method to that of the measured wind speed. The vertical axis is the wind speed difference estimated by each method, and the horizontal axis is the measured wind speed difference. The color represents each method, the colored line is the corresponding simple regression line, the dot is the site and target point and the gray line represents $y = x$.

Table 8 presents their statistical values. In Figure 9, the horizontal axis represents the true values based on measurement data, the vertical axis represents the estimated values for each method, the colors indicate the methods, each plot represents a case, and the line represents the regression line. Section 2.3.2 mentions that evaluations based on both differences and ratios aim to avoid method dependency; however, because both results were similar, this section focuses on the results for wind speed differences. The correlation coefficients of the regression lines for each method were sufficiently high ($\geq$0.89), revealing a clear relationship between the true values and estimates for each method. For CTRL, the slope of the regression line was 1.22, and the intercept was −0.08. Examining its individual cases revealed that three cases with relatively large horizontal wind speed differences showed a clear tendency toward overestimation. These cases were at low heights, and in order of the magnitude of the horizontal wind speed difference, they were St. B (Mutsu-Ogawara), SL (Noshiro), and VL (Noshiro). Comparing the slopes of the regression lines for each method, TC (1.12) was the closest to 1. Among the other methods, CTRL (1.22), NDG (1.25), and DE (1.38) followed in descending order of proximity to 1. Additionally, the intercept of TC's regression line was −0.04, the closest to 0, indicating the highest accuracy by considering the results of the slope. For the three cases with clear overestimation for CTRL, described above, the differences between methods were also relatively large and TC was the closest to the true value.

Table 8. Slope, intercept, and correlation coefficient of the regression coefficient for each method in Figure 9.

	Diff.			Ratio		
Method	**Slope**	**Intercept**	**R**	**Slope**	**Intercept**	**R**
CTRL	1.22	−0.08	0.90	1.32	−0.34	0.91
NDG	1.25	−0.06	0.88	1.35	−0.36	0.90
TC	1.12	−0.04	0.89	1.13	−0.14	0.92
DE	1.38	−0.08	0.89	1.38	−0.39	0.90

To illustrate this characteristic in detail, Figure 10 shows the frequency distributions of 10 min horizontal wind speed differences at each case. The horizontal axis represents the 10 min horizontal wind speed differences, while the vertical axis represents the frequency of occurrence. This figure shows that all 10 min horizontal wind speed differences reproduced by the four methods (CTRL, NDG, TC, and DE) had peaks in the positive range. However, the true values (OBS) based on the measurement data exhibited peaks closer to 0 m/s at most cases, with a relatively flatter distribution, indicating that the horizontal wind speed has a certain time variation. Among the four methods, DE exhibited a noticeably higher kurtosis and occurrences below 0 m/s were rarely observed in several cases. This suggests that when the reference point is located onshore near the coastline and the target point is offshore, applying wind speed ratios by direction alone may not adequately reflect the actual horizontal wind speed differences in terms of time variation. Conversely, WRF is characterized by its ability to reproduce time series, suggesting that applying temporal horizontal wind speed differences is superior to applying directional statistical metrics in reproducing horizontal wind speed differences. However, even the three methods—CTRL, NDG, and TC—exhibited relatively high kurtosis in their distributions compared with the observational values, indicating room for improvement in reproducibility.

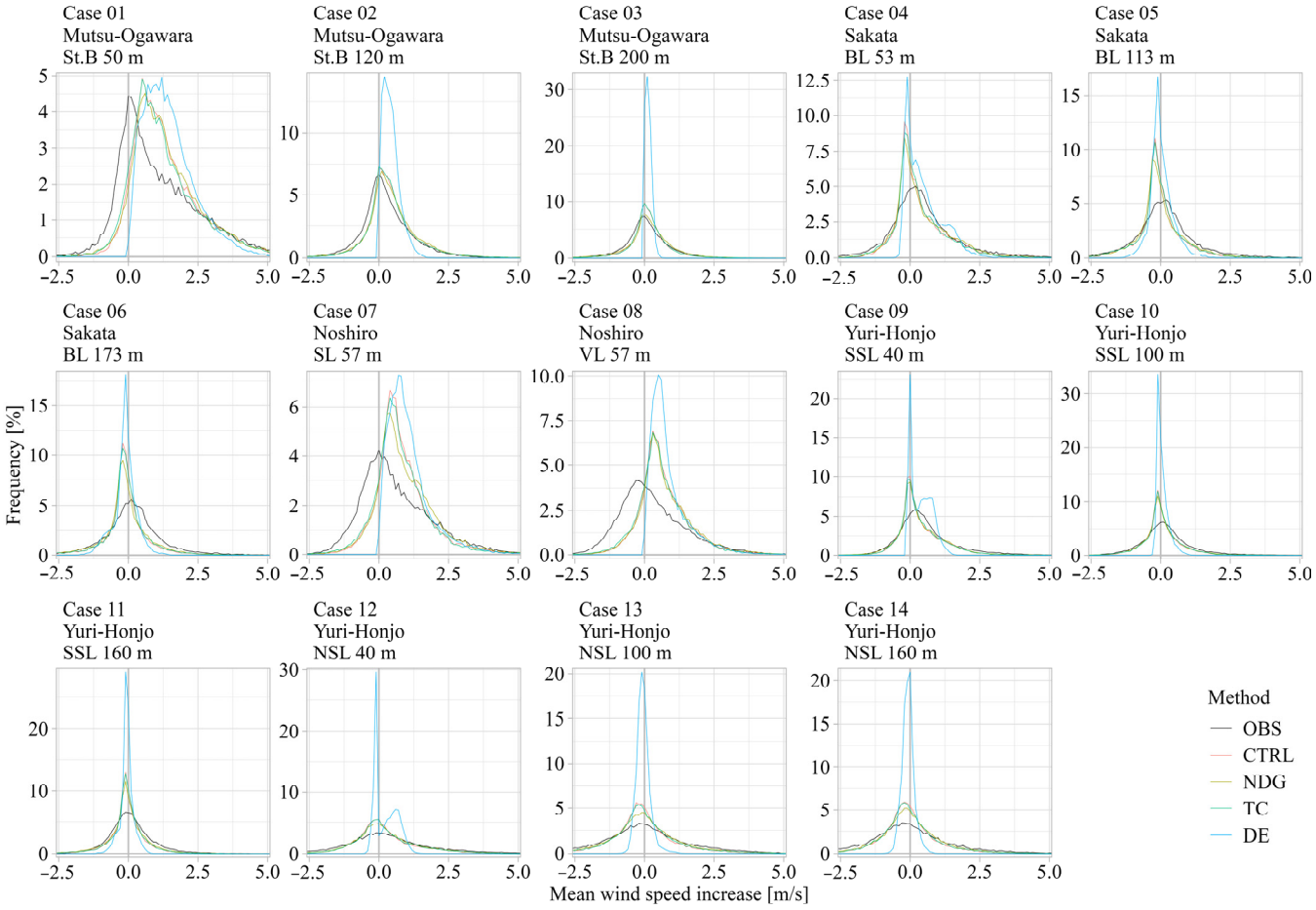


Figure 10. Comparison of mean wind speed difference frequency distributions across methods at each point and height. The vertical axis represents the frequency (%) of mean wind speed difference occurrences in 0.1 m/s bins (the scale of the vertical axis differs between plots), the horizontal axis shows the mean wind speed difference (m/s), the colors indicate estimation methods, and each figure corresponds to a specific estimation site and its height—a case.

In this section, the relationship between the wind speeds at the reference and target points was examined. First, NDG and CTRL were observed to include reference point biases that were not included in TC and DE. TC demonstrated the highest accuracy in reproducing wind speed differences, with the slope of the regression line being closest to the true value, followed by NDG, CTRL, and DE. It was suggested that DE, with its high kurtosis in the 10 min averaged wind speed difference distribution, may be limited in accurately capturing the actual horizontal wind speed differences.

3.3. Evaluation of KPIs That Consider the Characteristics of Each Site

Generally, wind condition estimation methods that use both measurement values and WRF models (in this study, NDG, TC, and DE) yield increased uncertainty in wind condition estimation as the relationship between the reference and target points weakens. In Figure 5, the distances between a reference point and the target point for these three locations are ordered as St. B (Mutsu-Ogawara), SL (Noshiro), and NSL (Yuri-Honjo), and the dispersion of the plot and R^2 for NDG, TC, and DE tended to decrease. These considerations confirm the need for accuracy evaluations based on the relationship between a reference point and the target point. While the explanation above was simplified using distance alone, various factors such as the surrounding terrain influenced the relationship. Therefore, in this study, the correlation coefficient based on the measured 10 min average

wind speeds between a reference point and the target point was adopted as an indicator to represent their relationship. The relationship between the correlation coefficient and distance is discussed in Section 4.

The relationship between the correlation coefficient and the coefficient of determination between a reference point and the target point was evaluated. The results are shown in Figure 11 and the corresponding statistics are presented in Table 9. The horizontal axis represents the correlation coefficient between a reference point and the target point of the measured wind speed, the vertical axis represents the coefficient of determination of wind speed for each estimation method, the colors indicate the different methods, and the plots represent the individual cases. The mean values for bins with a width of 0.05 (0.85–0.90, 0.90–0.95, 0.95–1.00, 1.00) are shown as circular markers and bars, with the error bars of the bars indicating the range of 1.28σ. The number of cases in each bin was 2, 5, 7, and 10, respectively, from the bin with the smallest correlation coefficient. Notably, the number of cases was small, particularly for the bin with a minimum value of 0.85. Additionally, the bin with a correlation coefficient of 1.00 represents the estimation results for the reference points.

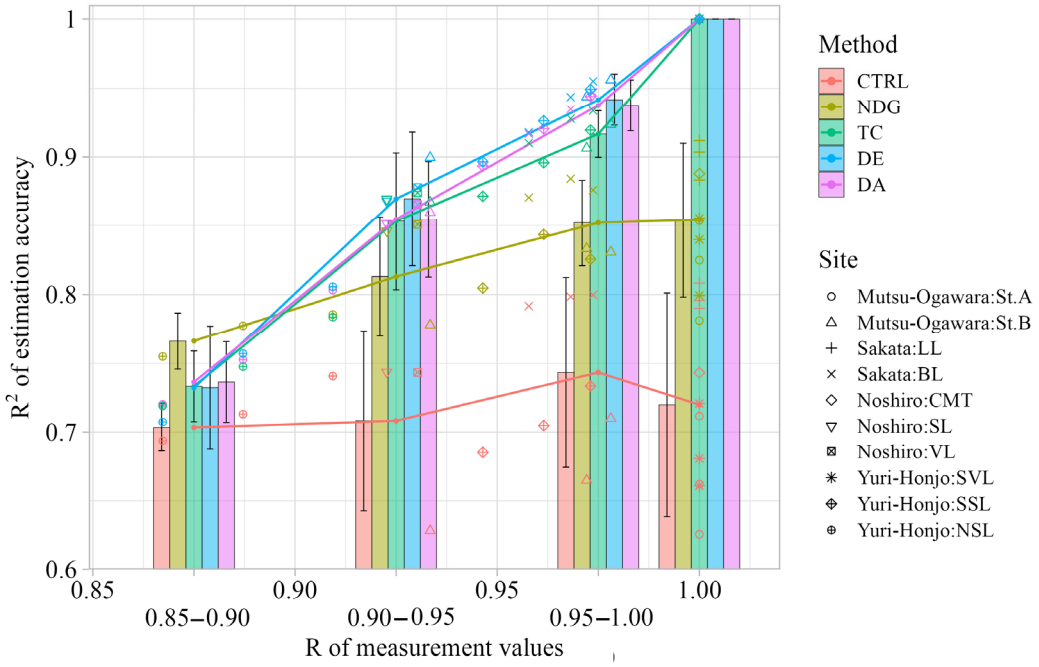


Figure 11. Scatter plot and its bin's mean values and standard deviation for R^2 of estimation accuracy of wind speed to the coefficient of determination between reference and target points of the measured wind speed. The vertical axis is R^2 of estimation accuracy of wind speed, and the horizontal axis is the R between reference and target points of the measured wind speed. The color represents the method, the shape of the dot is the target point, the colored line and the colored bar are the corresponding bin mean, and the error bar of the colored bar is the corresponding bin in the range of $\mu \pm 1.28\sigma$.

The mean value of CTRL, which is independent of the correlation coefficient between the reference and target points, showed values within a similar range (0.70–0.74) across all bins. The average coefficient of determination (R^2) for each method was compared across bins. In the 1.00 bin, DA, DE, and TC had an R^2 of 1 because the reference point was the target, and the reference and estimated values matched. NDG (0.85) was clearly higher than CTRL (0.72). In the 0.95–1.00 bin, DA and DE showed similarly high R^2 values (both 0.94), TC had a slightly lower value (0.92), and NDG had an even lower value (0.85). In the 0.90–0.95 bin, the three methods, DA (0.85), DE (0.87), and TC (0.85), showed little difference, and the gap between NDG (0.81) and the other three methods decreased.

Furthermore, in the 0.85–0.90 bin, NDG had the highest R^2 value (0.77), whereas DA (0.74), DE (0.73), and TC (0.73) had slightly lower R^2 values.

Table 9. Statistics for each method in Figure 11.

Bin of R			**0.85–0.90**					**0.90–0.95**		
# of Cases			**2**					**5**		
Method	**CTRL**	**NDG**	**TC**	**DE**	**DA**	**CTRL**	**NDG**	**TC**	**DE**	**DA**
Mean [%]	0.70	0.77	0.73	0.73	0.74	0.71	0.81	0.85	0.87	0.85
Std.Dev. [%]	0.01	0.02	0.02	0.04	0.02	0.05	0.03	0.04	0.04	0.03
Bin of R			**0.95–1.00**					**1.00 (Only reference points)**		
# of cases			**7**					**10**		
Method	**CTRL**	**NDG**	**TC**	**DE**	**DA**	**CTRL**	**NDG**	**TC**	**DE**	**DA**
Mean [%]	0.74	0.85	0.92	0.94	0.94	0.72	0.85	1.00	1.00	1.00
Std.Dev. [%]	0.05	0.02	0.01	0.01	0.01	0.06	0.04	0.00	0.00	0.00

Overall, a trend that was generally predicted was observed among the four methods that utilized the measurement data (DA, NDG, TC, and DE), where the coefficient of determination (R^2) decreased as the correlation coefficient between a reference point and the target point weakened, although the R^2 values were not smaller than those of CTRL in all bins. Among these methods, DE and TC exhibited a decrease in R^2, similar to that of DA, which directly uses measurement data. However, NDG showed a different characteristic compared to the other three methods, with relatively low R^2 values when the correlation coefficient was 0.90 or higher, but the highest R^2 values when the correlation coefficient fell below 0.90. This difference reflects the methodological distinction that, while DA, DE, and TC directly incorporate the temporal variability of measurement data at the reference point, NDG partially incorporates it through weighted calculations within its framework. This suggests that tuning the weighting coefficient α of TC to be less than 1 by considering the correlation coefficient between a reference point and the target point may increase the coefficient of determination (R^2) and improve the accuracy of TC.

4. Discussion

In Section 3.3, the correlation coefficient between a reference point and the target point, based on the measured 10 min mean wind speed, is used as an indicator to represent their relationship. In wind condition estimation, the distance is generally used as the standard parameter for evaluating this relationship. Therefore, this section examines the correlation between the correlation coefficient and the distance. Additionally, because height differences may influence the correlation, the analysis was conducted by classifying the data by height.

Figure 12 illustrates the relationship between distance and the correlation coefficient for the six target points relative to their reference points across the four sites, whereas Figure 13 presents this relationship categorized by height. As is commonly observed, the correlation tends to decrease as the distance increases. When categorized by height, a trend was observed where the correlation coefficient, plotted on the vertical axis, increased at greater heights. This suggests that at greater heights, the influences of the surrounding terrain and sea surface diminish, resulting in a more homogeneous wind field. Additionally, in the investigation described in Section 3.3, the evaluation was conducted without separately classifying cases of different heights at the same target point. However, using the correlation coefficient instead of distance between reference and target points can be considered a "normalized" evaluation that accounts for both distance and height differences.

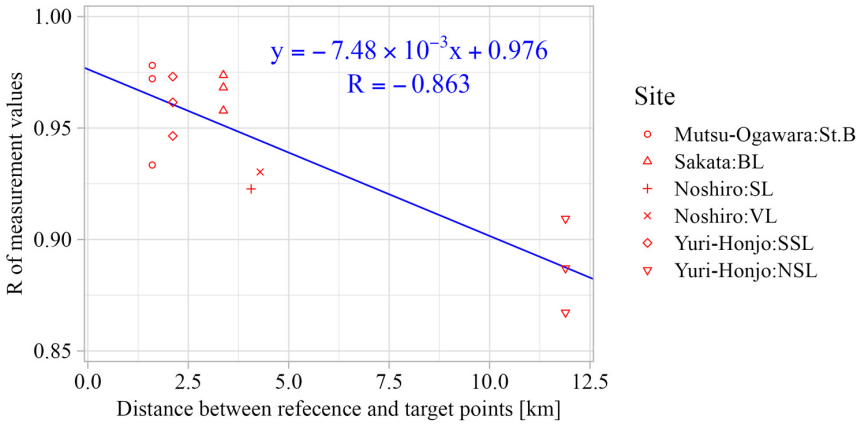


Figure 12. Relationship between distance and correlation coefficient (R) of measurement values across different sites. The vertical axis represents the correlation coefficient (R) of measurement values, while the horizontal axis shows the distance between reference and target points (km). Data from multiple sites—Mutsu-Ogawara (St. B), Sakata (BL), Noshiro (SL and VL), and Yuri-Honjo (SSL and NSL)—are displayed with site-specific markers. The blue regression line indicates the linear relationship, with the corresponding equation shown in the figure.

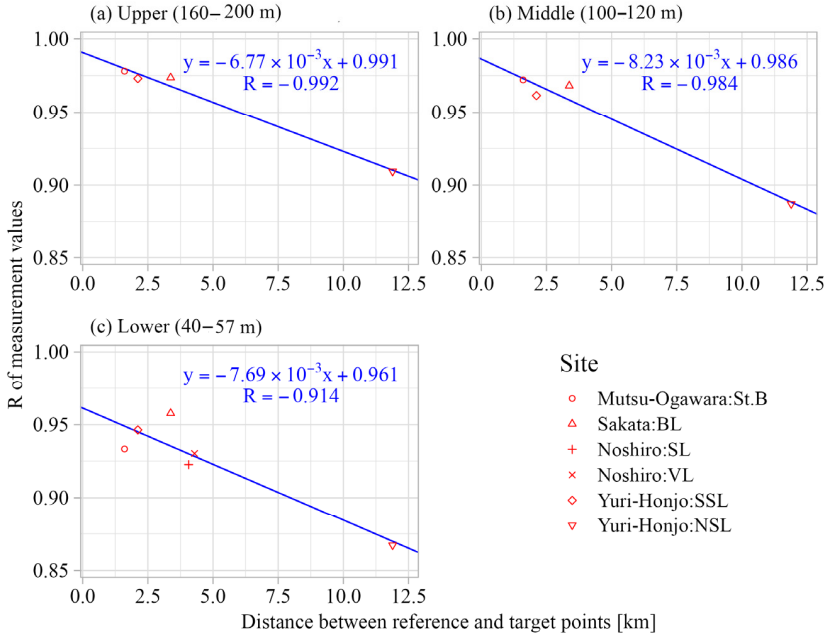


Figure 13. Relationship between distance and correlation coefficient (R) of measured values across different height categories. The vertical axis represents the correlation coefficient (R) of measurement values, while the horizontal axis shows the distance between reference and target points (km). The plots are divided into three height levels: (**a**) Upper (160–200 m), (**b**) Middle (100–120 m), and (**c**) Lower (40–57 m). Data from multiple sites—Mutsu-Ogawara (St. B), Sakata (BL), Noshiro (SL and VL), and Yuri-Honjo (SSL and NSL)—are shown with site-specific markers. The blue regression lines indicate the linear relationships, with the corresponding equations displayed in each figure.

Furthermore, the fact that the correlation coefficients remain high even at offshore points suggests that measurement at sufficiently high heights, considering the wind turbine hub heights, is crucial for offshore wind condition estimation. Moreover, this finding implies that referencing high-height measurements may enhance the estimation accuracy.

Until now, the uncertainty in wind estimation in wind resource assessment has generally been discussed in terms of topography and distance. However, if the correlation between the reference and target points can be estimated, it may be possible to directly

calculate the uncertainty of the wind condition estimation from the wind speed, without using topography or distance as parameters. This can be achieved by utilizing the results of wind condition estimation, which generates a time series using WRF.

5. Conclusions

The aim of this study was to clarify the characteristics of wind-field estimation by comparing the accuracy of several wind-field estimation methods using WRF and measurement data from a single point on land near the coastline. To achieve this, we examined five wind-field estimation methods: CTRL (WRF control simulation without on-site measurement data), NDG (observation nudging), TC (temporal correction method), DE (directional extrapolation method), and DA (direct-application method). Their accuracy in offshore wind condition estimation was evaluated using multiple performance indicators, including bias, RMSE, and the coefficient of determination (R^2), as well as by comparing the estimated horizontal wind speed differences and analyzing the relationship between the correlation coefficient (R) of the reference and target points and R^2.

First, we evaluated the bias of the estimated wind speeds. The results showed that TC demonstrated the highest accuracy, with the lowest mean bias (~0.0%) and the smallest standard deviation (2.6%), compared to 0.8–5.0% and 2.8–4.6%, respectively, for the other methods. Analysis of the slope of the regression line also indicated a similar trend. In terms of horizontal wind speed differences, the regression slope for TC was 1.12, closest to the ideal value of 1, indicating better agreement with the measured data. In contrast, the slopes for other methods ranged from 1.22 to 1.38. A frequency distribution analysis of the horizontal wind speed differences revealed that DE exhibited high kurtosis, leading to significant discrepancies with the measured values. In addition, CTRL, NDG, and TC did not achieve perfect agreement with the distribution based on the measurement data, indicating that each of these methods is affected by errors in the WRF simulation. Furthermore, it should be noted that CTRL and NDG exhibited bias not only at the target point but also at the reference point.

The analysis based on the coefficient of determination (R^2) of the wind speeds provided further insights into the method performance. DE, DA, and TC, with average values of 0.89, 0.88, and 0.87, respectively, exhibited high R^2 values, indicating that these methods performed well in predicting temporal variations in wind speed. As the correlation between the reference and target points decreased, the R^2 values for NDG, DE, DA, and TC also decreased. Notably, when the correlation coefficient (R) between the reference and target points dropped to around 0.85–0.90, the R^2 values for DE, DA, and TC decreased to 0.73–0.74, approaching the level of CTRL (0.70). This suggests that when R falls below 0.85, DE, DA, and TC may perform worse than CTRL, indicating that their effectiveness diminishes under weak site correlations. This implies that further analysis under lower correlation conditions may be necessary to clarify the effective range of measurement data.

Regarding wind direction estimation, there were no substantial differences among the examined methods, and all methods provided sufficient accuracy for practical wind resource assessment.

Among the methods considered, this study concludes that the temporal correction method (TC) provides the highest accuracy. However, the current form of the weighting function α used for spatial extrapolation in TC remains simplistic due to the lack of empirical validation. In the future, we plan to enhance the accuracy of the correction coefficients used in TC—specifically, the weighting function α for spatial extrapolation—and, further, develop a method that incorporates multiple onshore and offshore on-site measurement points, rather than referring to a single point for each development site.

Author Contributions: Conceptualization, T.M. and T.O.; data curation, T.M.; formal analysis, T.M.; funding acquisition, T.O.; methodology, T.M.; project administration, T.O.; resources, T.O.; software, T.M.; supervision, T.O.; validation, T.M.; visualization, T.M.; writing—original draft, T.M.; writing—review, and editing, T.O. All authors have read and agreed to the published version of the manuscript.

Funding: This study was supported by the Japan Society for the Promotion of Science (JSPS; Grant Number 17H03492 and 22H02018) and the New Energy and Industrial Technology Development Organization (NEDO; Grant Number JPNP07015).

Institutional Review Board Statement: Not applicable.

Informed Consent Statement: Not applicable.

Data Availability Statement: The data for this study can be obtained partly from the corresponding author upon request.

Acknowledgments: This study is based on observations obtained from several projects: the Ministry of the Environment (MoE) project conducted by the Japan Weather Association (JWA), the New Energy and Industrial Technology Development Organization (NEDO) project conducted by Kobe University and several organizations (JPNP07015), a measurement campaign by Japan Renewable Energy (JRE; ENEOS Renewable Energy at present), and a NEDO project conducted by the Japan Meteorological Corporation (JMC) and several organizations. This study used the supercomputer system at Kyoto University. The authors are grateful to all involved in these projects.

Conflicts of Interest: The authors declare no conflicts of interest regarding the publication of this paper.

Appendix A

All Statistics Indicators

Appendix A presents the tables of all KPIs for each method at the 14 target points (Tables A1 and A2), as mentioned at the beginning of Section 3 and the KPIs of CTRL and NDG at the reference points (Tables A3 and A4), as referred to in Section 3.2.

Table A1. KPIs of wind speed by five methods at target points in four sites.

Case	Height AMSL [m]	Rel. Bias [%]					Rel. RMSE [%]					Slope					R^2				
		CTRL	NDG	TC	DE	DA	CTRL	NDG	TC	DE	DA	CTRL	NDG	TC	DE	DA	CTRL	NDG	TC	DE	DA
Mutsu-Ogawara St. B distance: 1604 m																					
01	53	−3.4	−2.0	2.7	5.4	−16.6	32.4	24.8	19.5	17.6	27.0	0.92	0.94	1.00	1.03	0.81	0.63	0.78	0.87	0.90	0.86
02	113	−2.9	−1.7	2.0	2.1	−3.9	30.5	21.3	16.7	12.8	13.0	0.94	0.96	1.01	1.01	0.95	0.66	0.83	0.91	0.94	0.94
03	173	−2.8	−2.4	1.0	0.8	−1.3	28.4	21.5	14.7	10.9	10.9	0.94	0.96	1.00	1.00	0.98	0.71	0.83	0.92	0.96	0.96
Sakata BL distance: 3374 m																					
04	50	−6.5	−6.6	−1.9	0.4	−7.3	28.6	23.1	18.6	17.3	19.4	0.90	0.91	0.97	0.98	0.92	0.79	0.87	0.91	0.92	0.92
05	120	−5.4	−6.1	−2.4	−1.9	−2.9	28.4	22.4	17.3	15.1	16.4	0.91	0.92	0.97	0.97	0.95	0.80	0.88	0.93	0.94	0.93
06	200	−5.2	−6.7	−3.9	−3.8	−2.9	28.8	23.6	17.2	14.3	15.1	0.91	0.92	0.96	0.96	0.96	0.80	0.88	0.93	0.96	0.95
Noshiro SL distance: 4065 m																					
07	57	−4.1	−1.4	2.0	6.6	−10.5	26.0	19.9	19.7	21.7	22.8	0.93	0.96	1.01	1.06	0.90	0.74	0.85	0.87	0.87	0.85
Noshiro VL distance: 4290 m																					
08	57	−1.3	0.8	5.5	9.1	−5.7	26.5	20.3	20.9	22.8	20.6	0.96	0.99	1.04	1.08	0.94	0.74	0.85	0.87	0.88	0.87
Yuri-Honjo SSL distance: 2115 m																					
09	40	0.8	−1.6	−2.6	−2.5	−9.0	29.2	22.8	18.2	16.0	18.7	0.98	0.97	0.96	0.96	0.90	0.68	0.80	0.87	0.90	0.89
10	100	1.6	−1.3	−1.8	−2.1	−3.7	29.7	21.2	17.1	14.3	15.2	0.98	0.97	0.97	0.96	0.95	0.70	0.84	0.90	0.93	0.92
11	160	1.2	−1.8	−1.9	−2.2	−2.0	29.4	23.6	15.7	12.5	13.0	0.98	0.97	0.97	0.97	0.97	0.73	0.83	0.92	0.95	0.94
Yuri-Honjo NSL distance: 11,890 m																					
12	40	1.9	0.4	−0.5	−1.4	−5.8	29.4	26.1	27.5	26.7	27.5	0.98	0.97	0.95	0.94	0.90	0.69	0.75	0.72	0.71	0.72
13	100	3.7	1.5	0.9	0.0	−0.1	29.9	26.0	27.5	25.6	26.1	0.99	0.98	0.97	0.95	0.95	0.71	0.78	0.75	0.76	0.75
14	160	4.0	1.8	1.2	0.6	1.0	29.2	26.4	26.0	23.9	24.3	0.99	0.98	0.97	0.96	0.97	0.74	0.79	0.78	0.81	0.80
Mean		−1.3	−1.9	0.0	0.8	−5.0	29.0	23.1	19.8	17.9	19.3	0.95	0.96	0.98	0.99	0.93	0.73	0.83	0.87	0.89	0.88
Std. Dev.		3.5	2.8	2.6	3.8	4.6	1.6	2.1	4.2	5.2	5.6	0.03	0.02	0.03	0.04	0.04	0.05	0.04	0.07	0.08	0.08

Table A2. KPIs of wind direction by five methods at target points in four sites.

Case	Height AMSL [m]	Bias [deg.]					RMSE [deg.]					Slope					Intercept					R^2				
		CTRL	NDG	TC	DE	DA	CTRL	NDG	TC	DE	DA	CTRL	NDG	TC	DE	DA	CTRL	NDG	TC	DE	DA	CTRL	NDG	TC	DE	DA
Mutsu-Ogawara St. B distance: 1604 m																										
01	53	0.9	0.7	−0.1	−0.1	−0.7	35.0	25.7	16.4	14.4	14.4	0.99	0.99	1.00	1.00	1.01	4.0	2.7	−0.5	−1.0	−2.1	0.86	0.92	0.97	0.97	0.97
02	113	1.2	1.1	0.0	0.0	−0.5	32.3	19.4	13.7	11.5	11.5	1.00	1.00	1.00	1.00	1.00	1.2	0.4	0.3	0.1	−1.5	0.88	0.95	0.98	0.98	0.98
03	173	1.8	1.3	0.0	0.0	−0.4	29.6	20.3	11.6	9.1	9.2	1.01	1.01	1.00	1.00	1.00	−1.2	−0.7	0.0	0.3	−0.7	0.90	0.95	0.98	0.99	0.99
Sakata BL distance: 3374 m																										
04	50	0.2	−0.5	−3.2	−3.2	−3.7	40.7	31.8	25.9	24.7	25.0	1.06	1.06	1.05	1.06	1.04	−12.7	−12.4	−13.5	−17.1	−13.0	0.86	0.91	0.94	0.95	0.94
05	120	0.0	−1.5	−3.1	−3.1	−3.3	39.8	29.5	24.4	22.3	22.9	1.06	1.05	1.05	1.05	1.03	−13.4	−13.0	−12.8	−13.5	−10.5	0.86	0.92	0.94	0.95	0.95
06	200	0.2	−0.8	−2.8	−2.8	−3.3	38.1	29.3	22.8	20.2	21.1	1.06	1.06	1.04	1.04	1.03	−13.4	−13.1	−11.6	−11.0	−10.6	0.87	0.92	0.95	0.96	0.95
Noshiro SL distance: 4065 m																										
07	57	1.6	3.4	2.8	2.8	3.0	36.4	27.2	25.7	24.6	25.1	1.01	1.00	1.01	1.00	1.01	−0.9	2.5	−0.1	2.7	1.8	0.87	0.92	0.93	0.94	0.93
Noshiro VL distance: 4290 m																										
08	57	1.6	3.6	2.6	2.6	3.0	36.8	28.1	24.7	23.1	23.4	1.01	1.00	1.01	1.00	1.00	−0.8	3.8	0.3	3.1	2.9	0.87	0.92	0.94	0.94	0.94
Yuri-Honjo SSL distance: 2115 m																										
09	40	5.4	5.6	3.1	3.1	2.0	37.9	30.3	23.5	20.7	20.6	0.99	0.98	0.98	0.97	0.99	7.9	9.5	7.6	8.1	4.8	0.86	0.90	0.94	0.95	0.95
10	100	4.7	4.5	2.3	2.4	1.5	35.9	25.1	20.8	18.7	18.9	0.99	0.99	0.98	0.98	0.99	6.4	6.8	5.4	5.5	3.6	0.87	0.93	0.95	0.96	0.96
11	160	5.1	4.4	1.6	1.6	0.8	35.5	28.4	24.9	24.1	24.3	0.99	0.99	0.99	0.99	0.99	7.6	6.9	3.4	4.4	3.0	0.87	0.91	0.93	0.93	0.93
Yuri-Honjo NSL distance: 11,890 m																										
12	40	8.8	8.2	6.1	6.4	6.0	39.1	35.6	34.0	31.6	31.6	0.97	0.97	0.95	0.94	0.95	15.4	14.6	15.9	18.9	15.3	0.85	0.88	0.88	0.90	0.90
13	100	7.1	6.2	4.6	4.9	4.4	36.9	32.2	30.9	29.0	29.2	0.99	0.99	0.97	0.96	0.97	8.7	8.4	10.6	12.9	11.4	0.87	0.89	0.90	0.91	0.91
14	160	6.7	5.6	3.3	3.3	3.1	35.9	32.8	31.4	30.0	30.3	1.00	0.99	0.99	0.98	0.98	7.7	6.8	6.2	7.8	7.6	0.87	0.89	0.89	0.90	0.90
Mean		3.2	3.0	1.2	1.3	0.9	36.4	28.3	23.6	21.7	22.0	1.01	1.01	1.00	1.00	1.00	1.2	1.7	0.8	1.5	0.9	0.87	0.92	0.94	0.95	0.94
Std. Dev.		3.0	3.0	2.9	3.1	3.0	2.9	4.5	6.4	6.6	6.7	0.03	0.03	0.03	0.03	0.03	9.0	8.8	8.7	9.9	8.2	0.01	0.02	0.03	0.03	0.03

Table A3. Accuracy verification result of wind speed by CTRL and NDG at reference points in four sites.

Case	Height AMSL [m]	Rel. Bias [%]		Rel. RMSE [%]		Slope		R^2	
		CTRL	NDG	CTRL	NDG	CTRL	NDG	CTRL	NDG
Mutsu-Ogawara St. A									
01	50	−5.5	−6.0	29.6	22.5	0.92	0.93	0.79	0.88
02	120	−2.9	−3.5	27.6	18.6	0.94	0.95	0.80	0.91
03	200	−1.0	−2.1	27.1	19.6	0.95	0.96	0.81	0.90
Sakata LL									
04	53	−8.3	−7.5	32.6	25.1	0.88	0.90	0.63	0.78
05	113	−4.9	−4.2	30.2	19.9	0.92	0.94	0.66	0.85
06	173	−3.6	−3.2	28.0	21.7	0.94	0.95	0.71	0.82
Noshiro CMT									
07, 08	57	−8.0	−6.4	29.0	19.8	0.89	0.92	0.74	0.89
Yuri-Honjo SVL									
09, 12	40	3.6	1.2	31.3	23.6	1.00	1.00	0.66	0.80
10, 13	100	3.7	0.7	30.5	20.1	1.00	1.00	0.68	0.86
11, 14	160	3.3	0.3	29.7	22.2	1.00	0.99	0.72	0.84
Mean		−2.4	−3.1	29.6	21.3	0.94	0.95	0.72	0.85
Std. Dev.		4.6	3.1	1.7	2.1	0.05	0.03	0.06	0.04

Table A4. Accuracy verification result of wind direction by CTRL and NDG at reference points in four sites.

Case	Height AMSL [m]	Bias [deg.]		RMSE [deg.]		Slope		Intercept		R^2	
		CTRL	NDG	CTRL	NDG	CTRL	NDG	CTRL	NDG	CTRL	NDG
Mutsu-Ogawara St. A											
01	50	3.0	2.2	41.0	31.6	1.00	1.00	3.5	2.7	0.85	0.90
02	120	2.9	1.4	38.8	24.9	1.01	1.01	0.4	−0.3	0.86	0.94
03	200	3.1	1.6	36.7	26.4	1.01	1.01	0.1	−0.7	0.88	0.93
Sakata LL											
04	53	1.3	1.4	36.0	27.6	0.98	0.98	5.8	5.9	0.85	0.91
05	113	1.3	1.0	33.4	19.7	1.00	1.00	1.1	1.3	0.88	0.95
06	173	1.7	1.5	29.9	23.4	1.01	1.01	−0.8	0.5	0.90	0.93
Noshiro CMT											
07, 08	57	−1.3	0.1	39.7	27.2	0.99	0.99	0.0	1.9	0.85	0.92
Yuri-Honjo SVL											
09, 12	40	2.7	2.7	38.7	31.0	1.00	0.99	2.1	4.5	0.85	0.90
10, 13	100	2.7	2.0	36.5	25.2	1.00	1.00	1.9	2.0	0.86	0.93
11, 14	160	3.6	2.9	38.0	30.3	1.00	1.00	4.0	3.8	0.85	0.90
Mean		2.1	1.7	36.9	26.7	36.9	26.7	1.8	2.2	0.86	0.92
Std. Dev.		1.4	0.8	3.2	3.7	3.2	3.7	2.1	2.1	0.02	0.02

References

1. MEASNET. *Evaluation of Site-Specific Wind Conditions*; Version 3; MEASNET: Madrid, Spain, 2022; p. 64.
2. Climate Integrate. *Offshore Wind in Japan: Policy Agenda and Prospects*; Climate Integrate: Tokyo, Japan, 2024; Available online: https://climateintegrate.org/wp-content/uploads/2024/04/Offshore-Wind-in-Japan-EN.pdf (accessed on 27 June 2025).

3. Troen, I.; Petersen, E.L. *European Wind Atlas*; Risø National Laboratory: Roskilde, Denmark, 1989.
4. Dayal, A.; Prasad, A.; Deo, R.C. Wind Resource Assessment and Energy Potential of Selected Locations in Fiji. *Renew. Energy* **2021**, *172*, 292–307. [CrossRef]
5. Al-Deen, S.; Yamaguchi, A.; Ishihara, T. A Physical Approach to Wind Speed Prediction for Wind Energy Forecasting. In Proceedings of the Fourth International Symposium on Computational Wind Engineering, Yokohama, Japan, 16–19 July 2006; pp. 349–352.
6. Konagaya, M.; Ohsawa, T.; Mito, T.; Misaki, T.; Maruo, T.; Baba, Y. Estimation of nearshore wind conditions using onshore observation data with computational fluid dynamic and mesoscale models. *Resources* **2022**, *11*, 100. [CrossRef]
7. Uchida, T. Computational Fluid Dynamics Approach to Predict the Actual Wind Speed over Complex Terrain. *Energies* **2018**, *11*, 1694. [CrossRef]
8. Stull, R.B. *An Introduction to Boundary Layer Meteorology*, 1st ed.; Springer: Dordrecht, The Netherlands, 1988; ISBN 978-90-277-2768-8.
9. De Tomasi, F.; Miglietta, M.M.; Perrone, R. The growth of the planetary boundary layer at a coastal site: A case study. *Bound.-Layer Meteorol.* **2011**, *139*, 521–541. [CrossRef]
10. Floors, R.; Batchvarova, E.; Gryning, S.-E.; Peña, A. Atmospheric boundary layer wind profile at a flat coastal site—Wind speed lidar measurements and mesoscale modeling results. *J. Appl. Meteorol. Climatol.* **2011**, *50*, 1694–1705. [CrossRef]
11. Dörenkämper, M.; Optis, M.; Monahan, A.; Steinfeld, G. On the offshore advection of boundary-layer structures and the influence on offshore wind conditions. *Bound.-Layer Meteorol.* **2015**, *155*, 459–482. [CrossRef]
12. Lo Feudo, T.; Calidonna, C.R.; Avolio, E.; Sempreviva, A.M. Study of the Vertical Structure of the Coastal Boundary Layer Integrating Surface Measurements and Ground-Based Remote Sensing. *Sensors* **2020**, *20*, 6516. [CrossRef]
13. Milovac, J.; Ingwersen, J.; Warrach-Sagi, K. Multi-nested WRF simulations for studying planetary boundary layer height and structure across the coastal zone. *Tellus A* **2020**, *72*, e17674. [CrossRef]
14. Kikuchi, Y.; Fukushima, M.; Ishihara, T. Assessment of a Coastal Offshore Wind Climate by Means of Mesoscale Model Simulations Considering High-Resolution Land Use and Sea Surface Temperature Data Sets. *Atmosphere* **2020**, *11*, 379. [CrossRef]
15. Konagaya, M.; Ohsawa, T.; Itoshima, Y.; Kambayashi, M.; Leonard, E.; Tromeur, E.; Misaki, T.; Shintaku, E.; Araki, R.; Hamada, K. Estimation of Wind Conditions in the Offshore Direction Using Multiple Numerical Models and In Situ Observations. *Energies* **2025**, *18*, 3000. [CrossRef]
16. Misaki, T.; Ohsawa, T.; Konagaya, M.; Shimada, S.; Takeyama, Y.; Nakamura, S. Accuracy Comparison of Coastal Wind Speeds between WRF Simulations Using Different Input Datasets in Japan. *Energies* **2019**, *12*, 2754. [CrossRef]
17. Skamarock, W.C.; Klemp, J.B.; Duhia, J.; Gill, D.O.; Liu, Z.; Berner, J.; Wang, W.; Powers, J.G.; Duda, M.G.; Barker, D.M.; et al. *A Description of the Advanced Research WRF Model*; Version 4; NCAR Technical Notes; National Center for Atmospheric Research: Boulder, CO, USA, 2019.
18. Reen, B.P. *A Brief Guide to Observation Nudging in WRF*; Battlefield Environment Division, Army Research Laboratory: Adelphi, MD, USA, 2016; Available online: https://raw.githubusercontent.com/wrf-model/OBSGRID/master/ObsNudgingGuide.pdf (accessed on 29 June 2025).
19. Gryning, S.-E.; Batchvarova, E.; Floors, R. A study on the effect of nudging on long-term boundary layer profiles of Wind and Weibull distribution parameters in a rural coastal area. *J. Appl. Meteorol. Climatol.* **2013**, *52*, 1201–1207. [CrossRef]
20. Mylonas, M.P.; Barbouchi, S.; Herrmann, H.; Nastos, P.T. Sensitivity analysis of observational nudging methodology to reduce error in wind resource assessment (WRA) in the North Sea. *Renew. Energ.* **2018**, *120*, 446–456. [CrossRef]
21. Désert, T.; Knapp, G.; Aubrun, S. Quantification and correction of wave-induced turbulence intensity bias for a floating LIDAR system. *Remote Sens.* **2021**, *13*, 2973. [CrossRef]
22. Kotake, N.; Kameyama, S.; Kajiyama, Y.; Enjo, M. Performance analysis of Mitsubishi Electric's wind lidar in the measurement campaign at European test sites. In Proceedings of the WindEurope Summit, Hamburg, Germany, 27–29 September 2016.
23. Branlard, E.; Pedersen, A.T.; Mann, J.; Angelou, N.; Fischer, A.; Mikkelsen, T.; Harris, M.; Slinger, C.; Montes, B.F. Retrieving wind statistics from average spectrum of continuous-wave lidar. *Atmos. Meas. Tech.* **2013**, *6*, 1673–1683. [CrossRef]
24. Peña, A.; Mann, J. Turbulence measurements with Dual-Doppler scanning lidars. *Remote Sens.* **2019**, *11*, 2444. [CrossRef]
25. Simon, E.; Courtny, M. *A Comparison of Sector-Scan and Dual Doppler Wind Measurements at Høvsøre Test Station—One Lidar or Two? DTU Wind Energy Report E-0112*; DTU Library: Roskilde, Denmark, 2016.
26. Misaki, T. A Study on Improving the Accuracy of Coastal Wind Speeds Simulated by Mesoscale Model. Ph.D. Thesis, Kobe University, Kobe, Japan, 2020; p. 78.
27. Stauffer, D.R.; Seaman, N.L. Use of Four-Dimensional Data Assimilation in a Limited-Area Mesoscale Model. Part I: Experiments with Synoptic-Scale Data. *Mon. Weather Rev.* **1990**, *118*, 1250–1277. [CrossRef]
28. Qian, G.-W.; Ishihara, T. A novel probabilistic power curve model to predict the power production and its uncertainty for a wind farm over complex terrain. *Energy.* **2022**, *261*, 125171. [CrossRef]

29. Misu, Y.; Ishihara, T. Prediction of frequency distribution of strong crosswind in a control section for train operations by using onsite measurement and numerical simulation. *J. Wind Eng. Ind. Aerodyn.* **2018**, *174*, 69–79. [CrossRef]
30. Chai, T.; Draxler, R.R. Root mean square error (RMSE) or mean absolute error (MAE)?—Arguments against avoiding RMSE in the literature. *Geosci. Model Dev.* **2014**, *7*, 1247–1250. [CrossRef]
31. DNV GL; Frazer-Nash Consultancy; Multiversum Consulting; Fraunhofer IWES. *Carbon Trust Offshore Wind Accelerator Road Map for the Commercial Acceptance of Floating LiDAR Technology Version 2.0*; Carbon Trust: London, UK, 2018; p. 149.
32. Kvålseth, T.O. Cautionary note about R 2. *Am. Stat.* **1985**, *39*, 279–285. [CrossRef]

Disclaimer/Publisher's Note: The statements, opinions and data contained in all publications are solely those of the individual author(s) and contributor(s) and not of MDPI and/or the editor(s). MDPI and/or the editor(s) disclaim responsibility for any injury to people or property resulting from any ideas, methods, instructions or products referred to in the content.